FY21 Lawrence Livermore National Laboratory Experimental Programs at the Omega Laser Facility

P. L. Poole,[1] R. F. Heeter,[1] F. Albert,[1] N. Candeias-Lemos,[1] S. Clarke,[1] A. L. Coleman,[1] F. Coppari,[1] T. Döppner,[1] M. Hohenberger,[1] A. Lazicki,[1] S. Jiang,[1] S. F. Khan,[1] Y.-J. Kim,[1] A. Krygier,[1] M. J. MacDonald,[1] E. V. Marley,[1] D. Martinez,[1] M. Millot,[1] B. B. Pollock,[1] D. Rusby,[1] A. M. Saunders,[1] R. Smith,[1] C. Stan,[1] G. F. Swadling,[1] E. Tubman,[1] S. Zhao,[2] and A. B. Zylstra[1]

[1]Lawrence Livermore National Laboratory
[2]Lawrence Berkeley National Laboratory

In fiscal year 2021 (FY21), Lawrence Livermore National Laboratory's (LLNL's) High-Energy-Density Physics (HED) and Indirect-Drive Inertial Confinement Fusion (ICF-ID) Programs conducted numerous campaigns on the OMEGA and OMEGA EP Laser Systems. This was the 23nd year of national laboratory collaborative experiments at Omega since the Nova Laser at LLNL shut down in 1999 (Ref. 1), building upon prior collaborations. In FY21 overall, these LLNL programs led 459 target shots, with 234 shots using only OMEGA and 214 shots using only OMEGA EP. Approximately 30% of the total number of shots (57 OMEGA shots and 43 OMEGA EP shots) supported the ICF-ID Campaign, with the remaining shots dedicated to experiments for HED physics grouped as hydrodynamics and plasma properties campaigns (35 OMEGA-only shots and 21 OMEGA EP-only shots), materials (68 OMEGA and 78 OMEGA EP), and outputs and survivability (23 OMEGA). Highlights of the various HED and ICF-ID campaigns are summarized in the following reports.

In addition to these experiments, LLNL principal investigators (PI's) led a variety of Laboratory Basic Science Campaigns using OMEGA and OMEGA EP, including 39 target shots using OMEGA and 52 shots using OMEGA EP.

Overall, LLNL PI's led a total of 459 shots at LLE in FY21. In addition, LLNL PI's supported 123 basic science shots in collaboration with the academic community, including 18 National Laser Users' Facility shots or Academic/Industrial Basic Science shots, and 14 LaserNetUS shots led by university collaborators.

This work was performed under the auspices of the U.S. Department of Energy by Lawrence Livermore National Laboratory under Contract Number DE-AC52-07NA27344.

Thermonuclear Burn and High-Yield Campaigns

Investigating the Behavior of Diamond Under Shock Compression to Its Melting Line with Pyrometry

Principal Investigator: M. Millot
Co-investigators: Y.-J. Kim, R. Briggs, and P. M. Celliers

High-density carbon (HDC)—diamond—ablators are used in many ICF designs at the National Ignition Facility (NIF). Understanding the microphysics behavior of this material along the multishock compression path typical for ICF implosions is fundamental. Here we focus on elucidating the behavior of diamond under shock compression to its melting transition, near 10 Mbar. The specific goal for this study is to provide more-accurate data than the previous study by Eggert *et al*.[2] more than a decade ago and inform the possibility of lowering the adiabat in HDC implosions on the NIF by tightly benchmarking equation-of-state (EOS) models near the first shock state.

To document the melting temperature of diamond near 10 Mbar, we launched strong unsupported shocks in a planar package containing a diamond plate [Fig. 1(a)]. Using line-imaging Doppler velocimetry [VISAR (velocity interferometer for any reflector)] and streaked optical pyrometry (SOP), we were able to record high-quality data in the 6- to 20-Mbar range. Analysis is ongoing for the 13 data sets we collected. In addition, using quartz as an impedance-matching standard allowed us to collect high-precision shock pressure–density data along the Hugoniot to complement our previous work reported in Ref. 3.

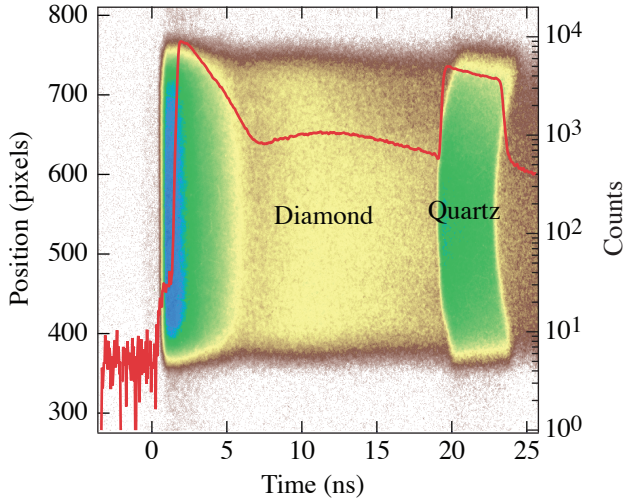

Figure 1
Example of a high-quality SOP image exhibiting sharp temporal and spatial resolution and a corresponding temporal lineout revealing a structured pyrometry signal indicative of a complex behavior under shock compression near 10 Mbar.

X-Ray Diffraction of Diamond Under Shock Compression and Shock-and-Release Near the Melting Line
Principal Investigator: M. Millot
Co-investigators: F. Coppari, D. Braun, A. Lazicki, Y.-J. Kim, P. M. Celliers, and J. H. Eggert

Using HDC—diamond—ablators in ICF implosions on the NIF has enabled important advances thanks to its efficiency as an ablator and the possibility to use shorter laser pulses.[4,5] However, the unique thermodynamic properties of carbon do present multiple challenges toward reaching higher fusion yield on the NIF. Among these challenges is whether rapid resolidification could occur after the first shock is transmitted to the hydrogen fuel and a release wave propagates backward toward the ablation front. Such a phenomenon would likely be a large source of implosion-quality degradation since the second shock would be launched into a slurry of nano-/microcrystalline diamond with a metallic fluid carbon.

Here we focus on elucidating the behavior of diamond under shock compression to completion of the melting line, near 12 Mbar, as well as under shock and subsequent decompression by an impedance-mismatch–generated release wave. The specific goal of this study is to characterize the atomic structure with *in-situ* nanosecond x-ray diffraction.

We launched strong steady shocks in a planar package containing a diamond plate mounted on the powder x-ray diffraction image-plate (PXRDIP) diagnostic box and collected high-quality x-ray diffraction data (Fig. 2) at unprecedented conditions in the 6- to 12-Mbar range. Ongoing analysis will allow us to reveal the atomic structure of carbon at those conditions and document the transition from the compressed solid to the metallic warm dense fluid.

Investigating Gold-Wall/Gas-Fill Interactions in an Open Geometry
Principal Investigator: G. F. Swadling
Co-investigators: E. Marley and W. A. Farmer

The AuGasJet-20 Campaign aimed to develop a new experimental platform to study the interaction of ablated gold plasma with a He gas fill. The overall purpose of this work is to benchmark simulations and therefore drive progress toward a predictive hohlraum performance model. The experiments use an open geometry, which provides excellent diagnostic access to the gold

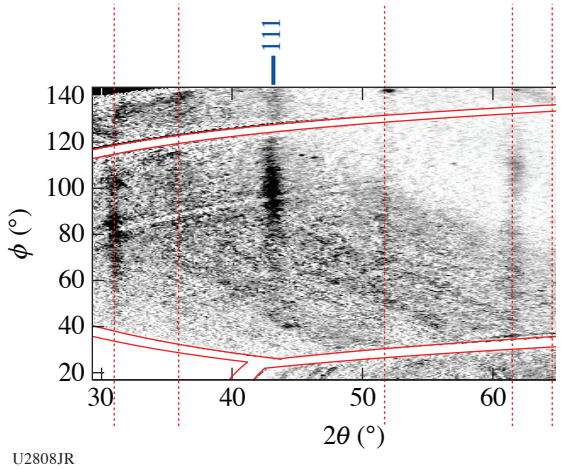

Figure 2
Example of a high-quality x-ray diffraction image exhibiting a strong line for shock-compressed diamond (indicated by the solid blue line) together with reference lines (dotted red vertical lines).

plasma, allowing detailed measurements of the plasma parameters of the gold and helium as they interact using the OMEGA 4ω Thomson-Scattering System (TSS). To achieve these goals, the experiments use a supersonic gas nozzle to inject a 0.3-mg/cm^3 plume of gas over the surface of a gold foil (see Fig. 3). The surface of the foil is then heated with the OMEGA 3ω heater beams, and the cloud of plasma that results is probed with Thomson scattering 300 μm from the foil surface. By using a gas jet, we aimed to remove the need for a "gas bag;" previous experiments using gas bags have shown that the shocks launched by the explosion bag wall significantly perturbs the experimental measurements. Using a gas jet also allows us to achieve ICF-relevant gas densities without resorting to a surrogate gas species or a cryogenic target design.

Two campaign days were scheduled in FY20 but the second day was delayed into FY21 when LLE shut down due to COVID. Thomson-scattering (TS) data collected in AuGasJet-20B was generally of a low quality. No signal was seen on a number of shots. We believe that the Thomson-scattering probe laser is struggling to penetrate the gold plasma plume produced in this experiment. This may be due to a more aggressive density gradient at the edge of this plume, compared to that produced in our previous experiments that have focused on probing plasmas ablated from spheres.

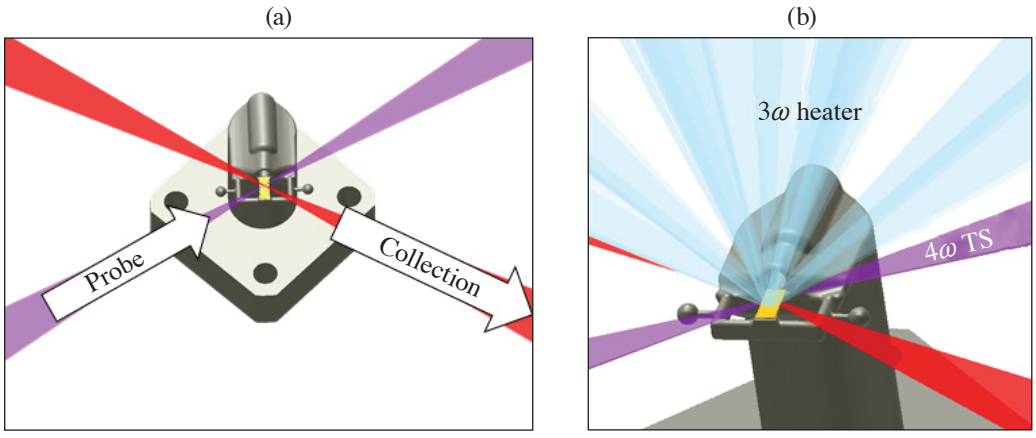

Figure 3
Experimental setup. A gas jet is used to produce a "gas fill" over the surface of a gold foil.

Assessing Heat Transport in the Transition Between Local and Nonlocal Regimes
Principal investigator: G. F. Swadling
Co-investigators: E. Marley and W. A. Farmer

In the BeSphere-21A Campaign, we performed experiments heating beryllium-coated spheres in a direct-drive geometry. The experiments were diagnosed using the OMEGA TSS, scatter calorimeters, and the Dante x-ray spectrometer. The aim of these experiments was to make quantitative measurements of the parameters of the blow-off plasma produced from these spherical targets. A total of 14 target shots were completed.

A previous campaign of experiments investigating beryllium spheres used comparatively low intensities of 1 to 2.5 × 10^{14} W/cm^2; at these intensities, coupling of the laser to the target was shown to be better than 90% (Ref. 6). On this most-recent shot day, heating intensity was increased from 5 × 10^{14} W/cm^2 to 1 × 10^{15} W/cm^2, comparable to the intensities at which we typically shoot ICF hohlraums.

The Thomson-scattering diagnostic measured the time-resolved spectrum of light scattered by fluctuations in n_e with wave vectors $\vec{k}$ tangential to the surface of the sphere. The size of the scattering volume, defined by the overlap of the probe beam and collection cone, was ~50 μm^3. Measurements were made at locations 200, 300 and 400 μm from the sphere surface. The diagnostic recorded scattering from both high-frequency electron plasma wave fluctuations (EPW, T_e, n_e) and low-frequency ion-acoustic wave fluctuations (IAW, T_e, T_i, v_{flow}). Examples of the data recorded are shown in Fig. 4. Fitting these measured spectra results in quantitative measurements of the plasma parameters, which may be compared with the results of numerical modeling.

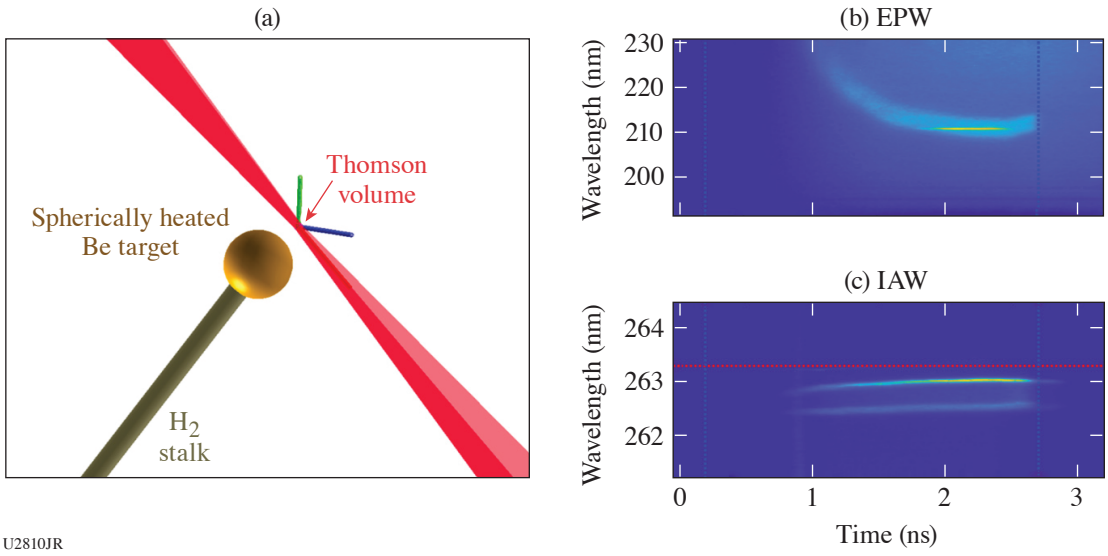

Figure 4
(a) Experimental setup and (b) example experimental data from BeSphere-21A.

Measurement of High-Z M-Shell Emission Using a Buried-Layer Platform
Principal Investigator: E. V. Marley
Co-investigators: R. F. Heeter, M. B. Schneider, G. E. Kemp, M. E. Foord, D. A. Liedahl, and J. Emig

This campaign was designed to measure the emitted M-shell spectra from well-characterized and uniform dysprosium and uranium plasmas to benchmark atomic kinetic models above and below the closed Ni-like subshell. The buried-layer target

geometry used for this experiment is capable of generating plasmas with an electron temperature of ~2 keV at electron densities of 1021 electrons per cubic centimeter. Similar plasmas are also found inside hohlraums during ICF experiments on the NIF, providing a stable platform to create uniform plasmas for radiation transport and atomic kinetic studies at relevant conditions.

Planar buried-layer targets were illuminated equally on both sides [Fig. 5(a)] to heat the sample. Two sample types were used during the campaign. The first was a 1400-Å-thick Dy/Cr mixture (0.27/0.73 by atom), and the second was a 1400-Å-thick U/Cr mixture. Both were designed to burn through completely before the end of the laser pulse, providing uniform plasma conditions to measure the M-shell emission of the high-Z component. The samples were buried between two 8-μm-thick layers of CH that acted as an inertial tamp that slowed the expansion of the sample.

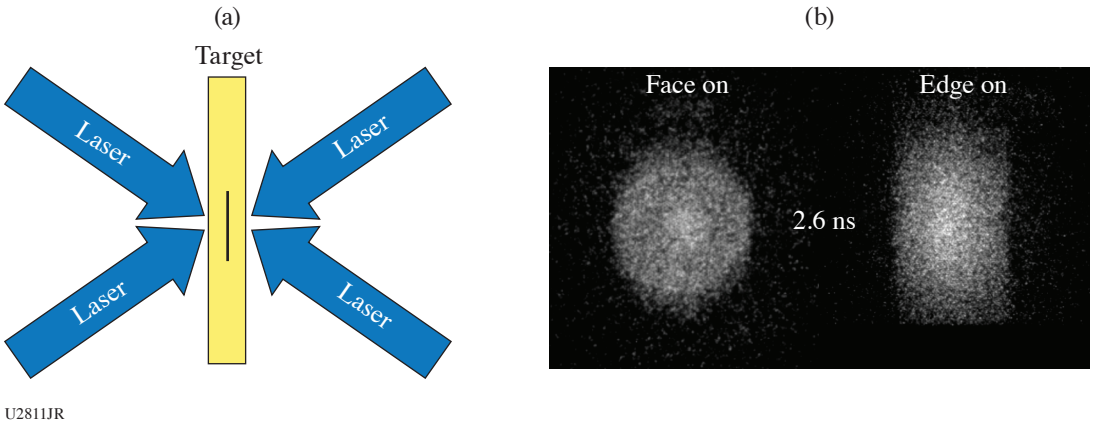

Figure 5
(a) Experimental configuration and (b) pinhole images of the emission area of shot 101947 at 2.6 ns.

Time-resolved 2-D images of the target's x-ray emission, viewed both face-on and side-on, were recorded using pinhole cameras coupled to framing cameras [see Fig. 5(b)]. The K-shell spectra from the Cr was used to determine the electron temperature of the plasma. The time-resolved spectra were recorded using crystal spectrometers coupled to framing cameras. Two crystal spectrometers were needed to record the 4 to 3 M-shell emission for both the Dy and the U, also time resolved. All of the framing cameras used, those for imaging as well as those for spectroscopy, were co-timed so the plasma conditions could be determined for the measured high-Z M-shell emission. A streak camera was also to be used to record a continuous record of the Dy M-shell emission, but it was not operational on the shot day.

The laser pulse shape used was a 3.0-ns square pulse with a 100-ps picket arriving 1 ns before the main pulse. A complete (five diagnostics, correctly timed and bias set) set of data was recorded for both target types, using both pulse shapes during the campaign at temperatures ~2 keV.

Plasma Growth on Nearby Targets During High-Intensity Laser–Plasma Interactions
Principal Investigator: D. Rusby
Co-investigators: N. Lemos and A. J. Mackinnon

High-intensity laser–plasma interactions are capable of creating high-energy particles/radiation including MeV x rays that can be used to perform nondestructive radiography of high-areal-density objects. Many laser-generated x-ray radiography scenarios use multiple interactions separated in time to either accumulate more x-ray dose or create several temporal snapshots. In such scenarios, the importance of understanding the effects of multiple interactions on one another is of utmost importance. The earliest interaction will produce high-energy x rays and electrons that can pre-ionize nearby targets, producing a pre-plasma that can greatly affect any subsequent interactions. Additionally, this interaction generates a large return current that can ionize the target stalk.

The OMEGA EP laser with 900 J and a 10-ps pulse duration was focused onto a 1 × 1-mm Ta cylinder used to generate x rays through bremsstrahlung. An additional identical target was placed ~1.5 mm away from the interaction. The additional target was held in place by either carbon stalks that are connected to the driven target or on its own separate target stalk. The 4ω probe was used to qualify the growth of the plasma on each of the targets. Two shots were taken using a separate target setup with the 4ω probe timed at 3 ns and 6 ns after the main interaction. One shot was performed on the connected targets with the probe timed at 3 ns. Composite images of the reference and on-shot data are shown in Fig. 6 to highlight the areas of plasma produced.

The plasma growth on the connected target is much greater than that of the separated targets. This is likely due to the return current that runs through the connected target stalks. The plasma that is generated on separated targets is directional. The side of the target that is facing the interaction of the driven target has much more plasma growth than the side that faces away. With the two scenarios investigated here, the preferable one for multiple laser interactions would be the separated targets. This investigation of plasma growth on targets has shown that with sequential high-intensity laser interactions, the choice of the target geometry will play a huge role. Simulations are being conducted to validate the results shown here, and further geometries, including shields, are being proposed and simulated.

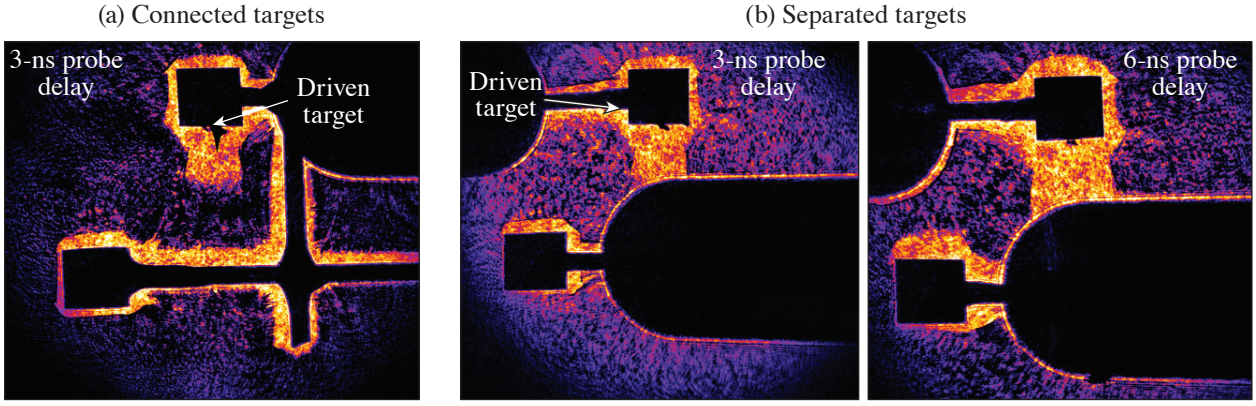

Figure 6
Composite 4ω optical probe images of the reference and on-shot data showing the growth of the plasma on (a) connected targets and (b) separated targets.

Shock-Propagation Measurements in Gas-Tube Targets with MIFEDS-Based Magnetic Fields
Principal Investigator: B. B. Pollock (LLNL)
Co-investigators: H. Sio, E. Marley, and J. D. Moody (LLNL); and J. R. Davies, P. V. Heuer, J. L. Peebles, and D. H. Barnak (LLE)

The goal of the BLoopEOS Campaign is to measure changes in shock-propagation speed and plasma preheat in the presence of preimposed magnetic fields. For the FY21 experiments, the imposed B field is provided by dual magneto-inertial fusion electrical discharge system (MIFEDS) coils supplying 20- to 25-T B fields in a gas-filled tube target, similar to the shock-tube target used in previous ProtonShockEP Campaigns. One end of the tube is sealed with a 50-μm CH ablator, which is driven by three overlapping long-pulse beams from OMEGA EP, as shown in Fig. 7. This launches a shock into the gas-filled tube (mixtures of He and Ne) with the B field perpendicular to the shock-propagation direction. The shock-propagation speed is expected to increase with increasing applied B field. In addition, the B field in the shocked region is calculated to increase due to compression by the same amount because the compression of the plasma density provided by the field is frozen into the plasma just ahead of the shock. The system is probed perpendicular to both the shock propagation and the B field by target normal sheath acceleration (TNSA)-driven proton radiography. The MIFEDS is designed to allow the direction of the magnetic field to alternate between "up" and "down" in the side-on view, changing the net direction of proton deflection from the Lorentz force. This results in changing the proton deflection direction to being predominantly away from the shock front or toward it, respectively, which changes the structure of

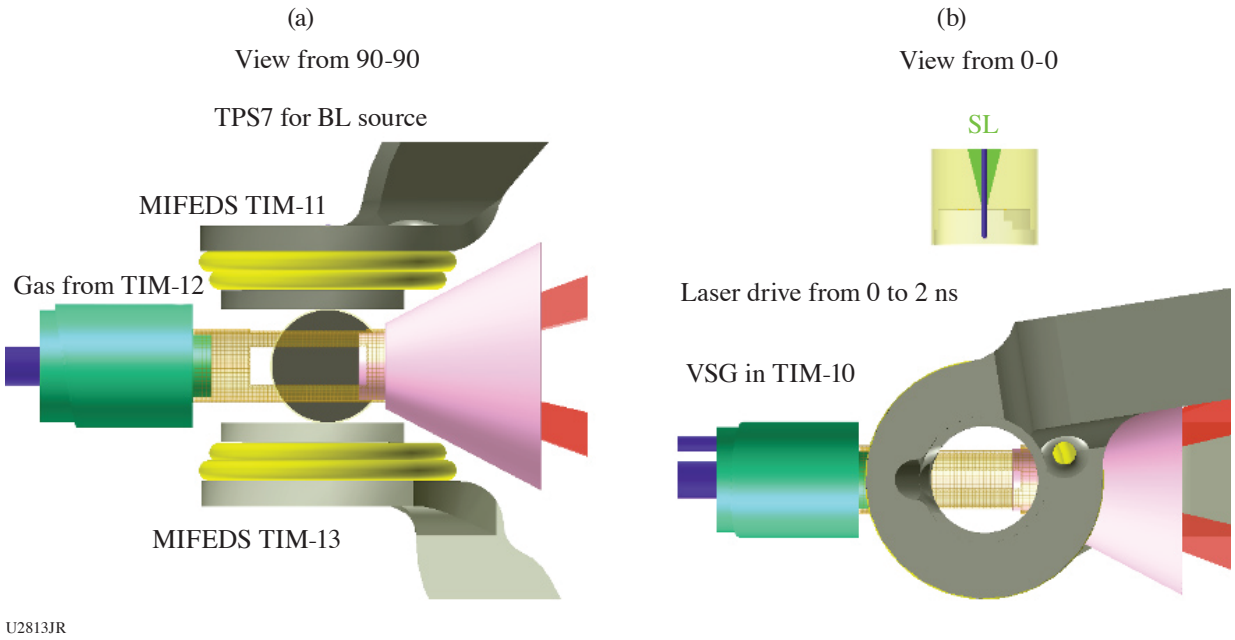

Figure 7
Experimental configuration showing the gas tube, the MIFEDS, the laser drive direction (here right to left), and the proton source. TIM: ten-inch manipulator; TPS: Target Positioning System.

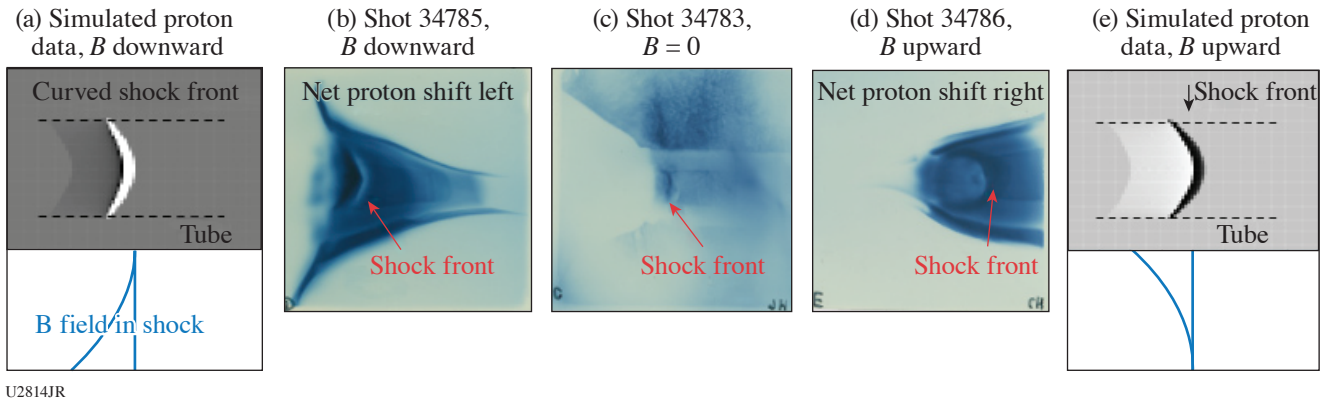

Figure 8
Proton radiography from two magnetized experiments with B fields applied in opposite directions and from one unmagnetized shot for reference. The magnetized shots are accompanied by calculated proton deflection images showing qualitative agreement to the data with respect to the brightness and curvature near the shock front. Here the laser is propagating from left to right.

the radiograph near the shock front. This can be seen in Fig. 8, where for shot 34785, the protons are shifted toward the ablator, resulting in a proton void at the shock front, while for shot 34786 the opposite is true. The proton data can be approximately reproduced in simulated proton images by assuming the shock amplifies the background field about a factor of 3 (from 20 T to 60 T). The shock is curved because of the small 400-μm laser spot size, and the B-field amplification is lower toward the shock edges. Spectroscopic measurements from the Ne emission along the length of the tube [recorded by the virtual synchronous generator (VSG) system] may show a shock-speed increase from 160 μm/ns to 220 μm/ns with the application of the B field as shown in Fig. 9. The speed increase is approximately the same for a B field "up" or "down," which is the expected result. These results are encouraging, and further analysis of both measurements is in process.

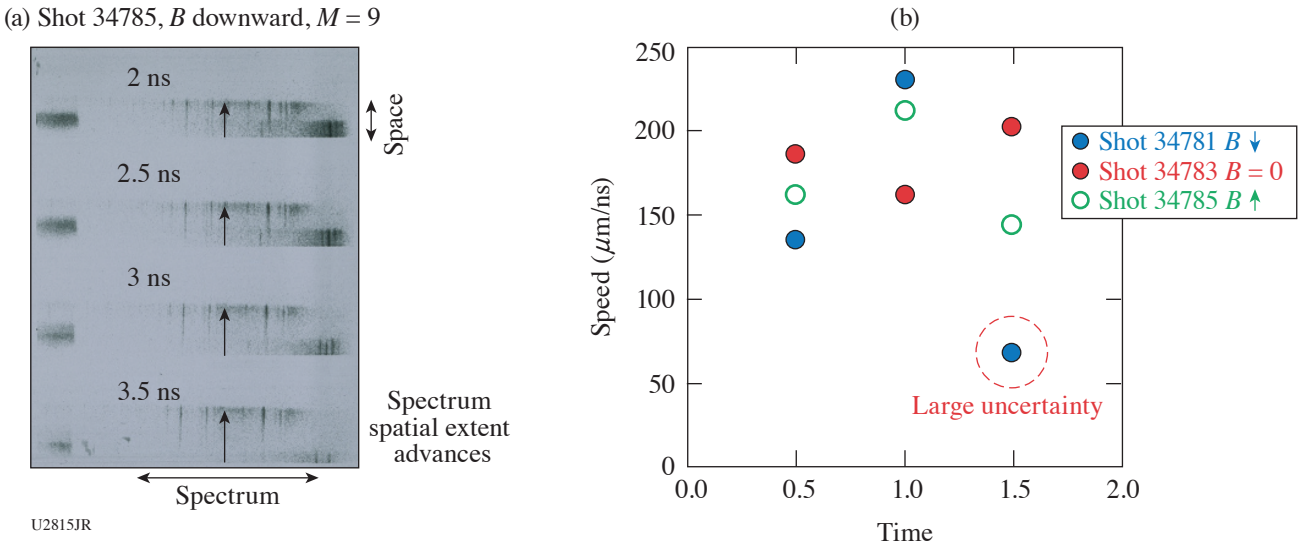

Figure 9
X-ray framing camera measurements of the spectral emission from the Ne recorded by VSG and the extracted propagation velocities for three shots with B = 0, B upward, and B downward.

High Current Generation Based on Capacitor-Coil, Laser-Driven B-Field–Generation Techniques for a Magnetically Insulated Transmission Line

Principal Investigator: B. B. Pollock (LLNL)

Co-investigators: D. Welch (Voss Scientific), P. V. Heuer (LLE), and K. LeChien (LLNL)

The use of high-power laser drivers to produce large (~100's T) magnetic fields in capacitor-coil–style targets has been studied and reported by several groups.[7–11] The fields are the result of high current flows that are sourced by voltage differences between electrically connected parallel plates when one plate is irradiated by a high-power laser and hot electrons leaving the driven surface leave behind a positively charged region; an example is shown as an inset in Fig. 10(a). The MiniMITL Campaign takes advantage of this voltage-generation scheme, with a goal of maximizing the current density through a return post between the parallel plates of the system. Many prior works have generally used either a single laser driver or several beams focused close together to generate the initial voltage difference across the capacitor-coil target. The survey of Refs. 7–11 in Fig. 10(a) indicates that the voltage difference scales somewhat weakly with the intensity of the laser driver, reducing the efficacy of overlapping laser spots for increasing voltage (and current). Simulations using the geometry of Figs. 10(b) and 10(c) have recently demonstrated that for multiple laser spots uniformly distributed azimuthally at a fixed radius on the driven plate, it is possible to increase voltage and current nearly linearly with a number of drivers for appropriate spot-to-spot spacing. Figure 10(d) shows the effect of increasing the number of laser beams at 4-mm radius, with each beam intensity at 2 PW/cm^2. Up to about four beams, the voltage increases approximately linearly, then more slowly with additional beams. This is due to the separation between the spots becoming smaller with more beams at fixed radius and spot size. This behavior is also seen in Fig. 10(e), where the current for eight beams is shown to increase quickly up to ~2-mm radius and then saturates.

The OMEGA EP Laser System is ideal for studying the current generation scaling from this scheme. MiniMITL21A uses up to all four of the OMEGA EP long-pulse beams to drive the rear plate of the target, with the beams pointed 90° apart from one another at a radius of 4.5 mm. The OMEGA EP pulse-shaping capability allows the laser intensity to be varied during the shot day, as well as the number of beams used in a single experiment. The primary diagnostic of the current through the return post is VISAR, viewing the exterior of the rear (driven) target plate, where the $J \times B$ forces of the current in the post and the induced azimuthal B field around it launch a shock in the plate. Ultimately four shots were successfully completed, but all in compromised targets due to damage from the shipping process. Despite that, some conclusions can still be drawn about the target design to

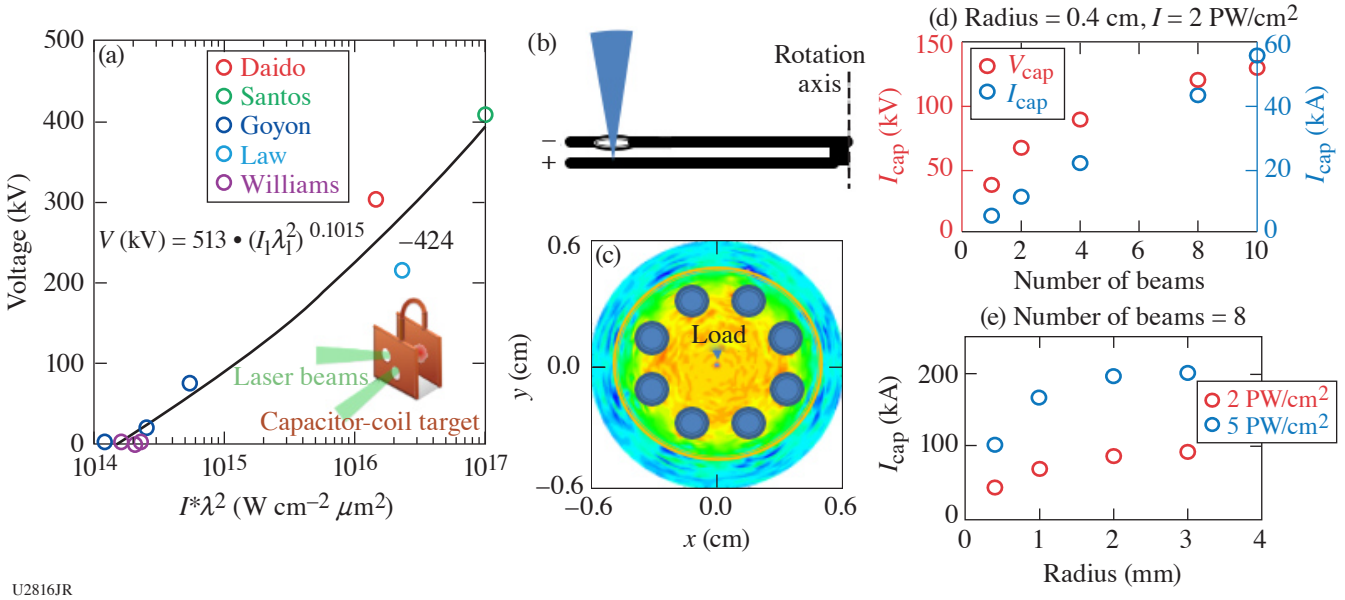

Figure 10
(a) Voltage as a function of laser intensity (and wavelength) for several published laser-driven B-field experiments. (b) Side-on profile of the MiniMITL target design, where the lower plane is laser driven to produce the initial voltage difference across the target. (c) Face-on profile of the target design, showing multiple laser spots uniformly azimuthally distributed around the driven plate at fixed radius from a return current post connecting it to the undriven side of the target [the rotation axis of part (b)]. (d) The driven voltage and current as functions of the number of drive beams at a fixed radius and beam intensity. (e) The driven current as a function of beam radius at two laser intensities.

make improvements for future shot days, both in terms of target survivability and diagnostic return. Additional shots have been requested for FY22 and will be again for FY23.

Modifications to Laser Scattering in Magnetized Plasmas
Principal Investigator: B. B. Pollock
Co-investigators: Y. Shi, E. Tubman, and J. Moody

Classical laser scattering in a plasma follows a dipole radiation pattern that is maximized perpendicular to the laser polarization and zero parallel to it. In the presence of strong magnetic fields (~100's of T), however, the orbits of oscillating electrons can be sufficiently perturbed to result in appreciable scattering in the initial laser polarization direction. The MagLoopLPI Campaign seeks to study this modified scattering using a laser-driven magnetic-field source[12] to provide a strong background magnetic field in a foil blow-off plasma. To produce the magnetic field, a loop target similar to that described in Ref. 12 is driven by one long-pulse beam of the OMEGA EP Laser System as shown in Fig. 11(a). The target has been modified from Ref. 12 by removing material from the center of the B-field loop to be able to position a foil target within the highly magnetized region. Additionally, this target is being driven on an external surface to limit the x-ray and plasma expansion to the vicinity of the foil; an additional "awning" is also placed in the line of sight from the B-field drive laser spot to the foil to further prevent preheating and plasma filling of the loop region. A CH foil is then positioned such that it can be irradiated by a second long-pulse beam, and the expanding plasma plume will have the laser-driven B field pre-embedded as it moves along the B-field lines (quasi-parallel to the foil normal).

To probe the foil plasma, the short-pulse beams of OMEGA EP are focused 200- to 300-μm from the foil surface using the backlighter parabola (where in "co-prop" mode, both short-pulse beams are available). The probe pulse is ~100 ps and ~1 J so that the probe will be minimally perturbative to the plasma conditions of interest. New diode systems, designed for use in this configuration, will be positioned along the vectors shown in Fig. 11(b). There is one diode along the laser polarization direction

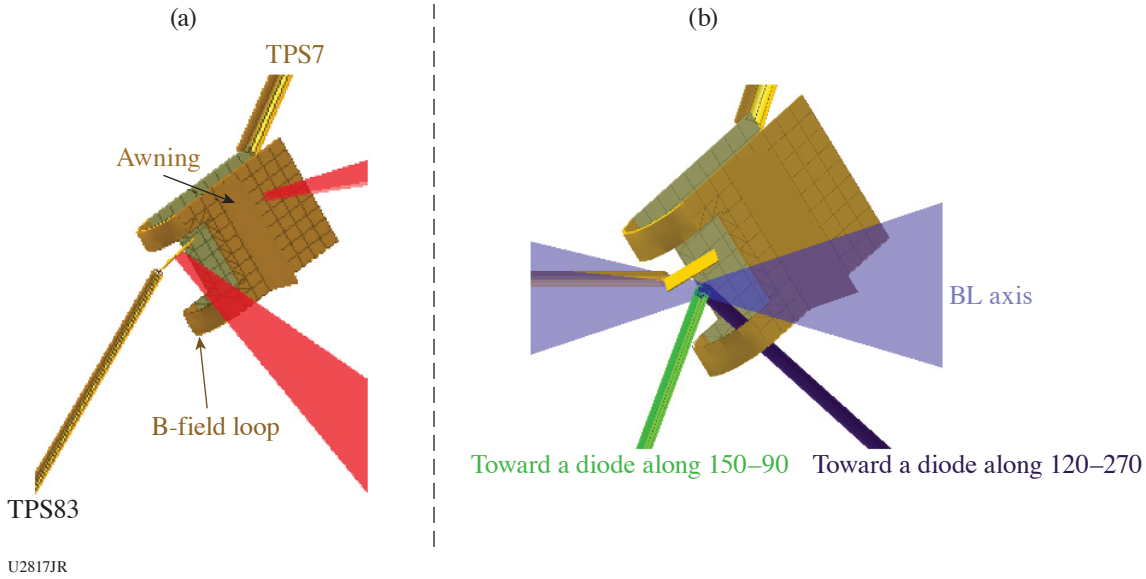

Figure 11
(a) The B-field loop target is shown with the CH foil, along with their respective drive beams. (b) The drive beams have been suppressed to show the optical probing geometry for the short-pulse beams on the backlighter axis. The rods toward chamber coordinates of 150–90 and 120–270 indicate the directions to the new diode diagnostics.

and one perpendicular to make simultaneous scattering measurements in these directions; in the co-prop mode where both short-pulse beams are available, the polarization can effectively be rotated 90° between shots (since the two beams in this geometry are cross polarized). This configuration also allows switching to a B-field characterization setup with minimal beam modifications (the short-pulse beam is refocused and the power increased) to enable proton probing of the magnetic-field structures at the target. Due to qualification issues, the diodes were not fielded on MagLoopLPI21A, but the proton-probing setup was successfully used for six target shots. Figure 12 shows representative proton radiography from three separate conditions: (1) where only the foil was

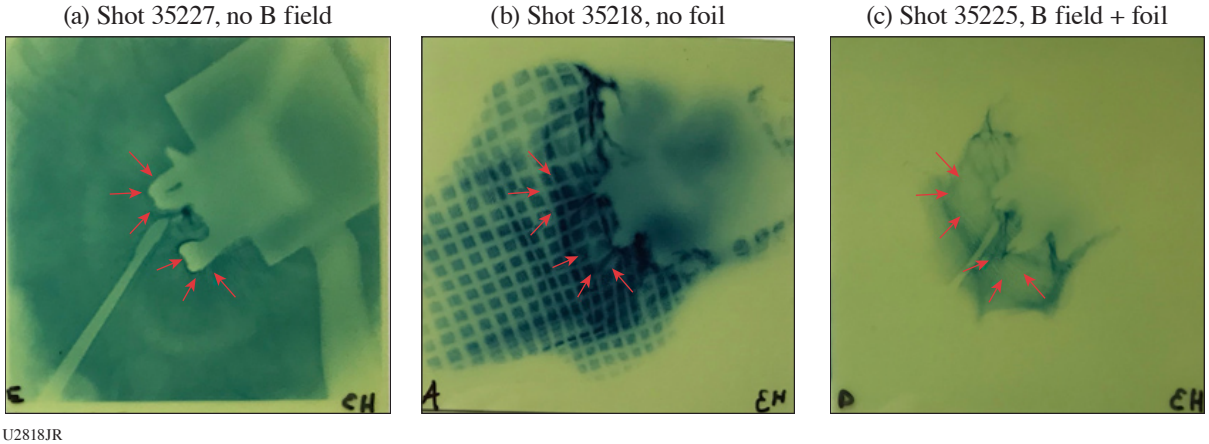

Figure 12
Proton radiography data from three separate shots. (a) Shot 35227 had no B field, but did drive the foil between the loops. The red arrows indicate the shadows from the current loops in the B-field target it is undriven. (b) Shot 35218 produced a B field (estimated ~100 to 200 T based on previous experiments with similar drive). The Lorentz force on the protons is such that they are pulled inward toward the loops, where grid-line distortion near the arrows shows protons moving inward. The grid and foil could not be fielded simultaneously. (c) Shot 35225 corresponds to the foil being driven with a B field applied. Detailed analysis is underway for all shots.

driven, (2) only the B field was driven (allowing for a grid to be inserted), and (3) where both targets are irradiated. Additional shots have been allocated for FY22 to make the scattering measurements (allowing time to clear the diode qualification issues), and these radiographs have also led to several modifications to the targets for the follow-on day. First, the shadows of the current loops are clearly visible in the radiograph from shot 35227, as highlighted by the red arrows. When the magnetic field is applied, the Lorentz force on the protons pulls them toward the loops, complicating the analysis. In comparison, in previous experiments (cf. Ref. 12), the field direction was reversed and protons were pushed outward from the target; the size of the void region was then directly related to the strength of the B field. For FY22, the driven portion of the target will be modified to maintain the x ray and plasma blocking for the foil but to recover the previous B-field direction for proton probing. Additionally, while analysis is still ongoing for the proton data, there is evidence in the radiographs from shots 35218 and 35225 that the field structure is very complex in the region of the foil. At the expense of total field, the FY22 targets will return to the solid-loop target geometry and position the foil just outside this region. The primary measurement will be the scattering, but these changes should improve future radiography measurements as well.

Scaling of Multipicosecond Deuteron Acceleration for the Development of a Laser-Driven Neutron Source
Principal Investigator: G. G. Scott (LLNL)
Co-investigators: D. A. Mariscal, E. Folsom, R. F. Heeter, R. J. Wallace, E. S. Grace, R. A. Simpson, and T. Ma (LLNL); and D. Canning, S. T. Ivancic, and M. Krieger (LLE)

The well-known d(^{7}Li,n)^{8}Be has been subject to a number of laser-driven neutron-production investigations since it is a mechanism that produces a highly directional and energetic neutron beam, owing to the extremely exothermic nature of the reaction, and a pulsed neutron source with such properties might find use for a myriad of applications. To efficiently drive such a neutron beam, efficient acceleration of a deuteron flux above the ∼4-MeV activation energy of reaction is crucial. To this end, our experiment aims to investigate the first detailed scaling of deuteron acceleration from a CD foil as a function of laser energy, intensity, and pulse duration while simultaneously using a portion of the deuterons to drive neutron generation via a pitcher/catcher configuration. This study is inspired by recent results on the scaling of laser-driven proton acceleration in the multipicosecond regime,[13] where ∼10-ps pulses were found to offer an optimum between drive time and laser pulse energy for optimal proton acceleration.

With deuterons being accelerated via TNSA, in the target normal direction, and with the D(^{7}Li,n) reaction known to have a strong directionality, a plasma mirror platform[14] was utilized such that sidelighter and backlighter-only shots could be directed to a target with a fixed diagnostic orientation with respect to the target, and ion acceleration was diagnosed by the TIM-based Thomson parabola ion energy (TPIE) diagnostic fielded in the target normal direction.

Preliminary experimental data analysis presented in Fig. 13(a) shows that the maximum deuteron energy is primarily dependent on the laser energy driving the acceleration, with laser intensity being less important. As the driving pulse duration increases, the energy partition in deuteron beam compared to that of the simultaneously accelerated proton beam also increases. Higher-energy, longer-duration laser pulses, therefore, appear to be beneficial for increasing the efficiency of deuteron acceleration, and numerical modeling will be conducted to understand the acceleration dynamics, and data obtained from the OU-ESM (Osaka University electron spectrometer) and neutron times of flight will further inform us on this study.

Hydrodynamics and Plasma Properties Campaigns

Mix-Width Measurements of Metallic Foams
Principal Investigator: D. A. Martinez (LLNL)
Co-investigators: S. F. Khan, T. Dittrich, S. G. Glendinning, R. J. Wallace, and T. Baumann (LLNL); and T. Woods, W. Man, and M. Arend (LLE)

This experiment series was designed to determine if the Ta_2O_5 foams at 0.85 g/cm^3 produce a smaller mix width compared to the previous mix-width data obtained with 0.9-g/cm^3 Cu foams due to the smaller cell size. For Ta_2O_5, the cell size is estimated

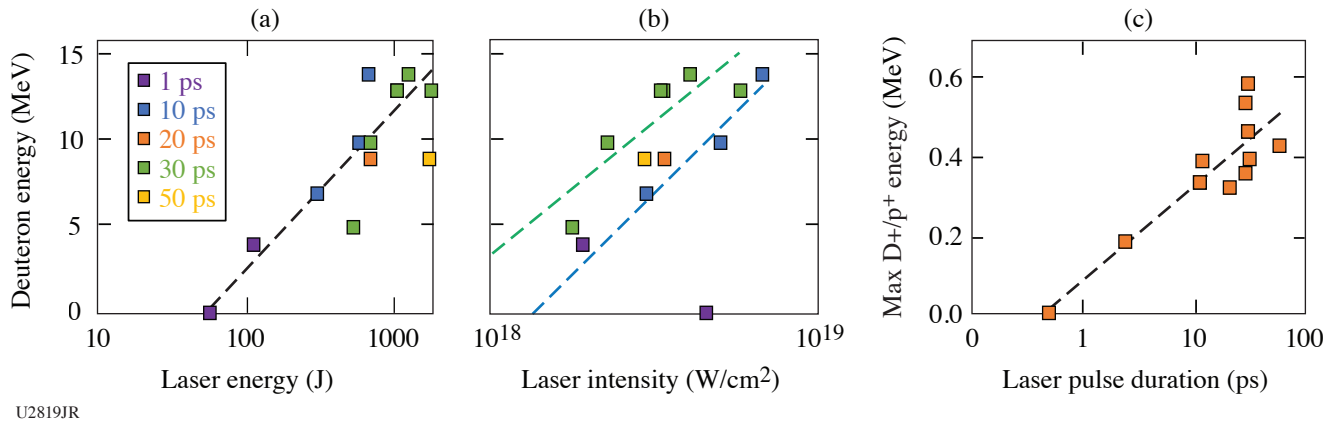

Figure 13
The maximum deuteron energy recorded on TPIE as a function of pulse duration and (a) laser energy and (b) laser intensity. (c) The ratio of maximum deuteron energy to proton energy as a function of pulse duration.

between 10 and 100 nm, while the Cu foams have a 1-μm cell size using a slip casting method. It is assumed that the cell size is the main seed for mix instabilities for foams.

The FmGrow-21A experiment used a half-hohlraum connected to a shock tube. The shock tube consisted of a polyethylene ablator and a metallic foam sample of Ta_2O_5 at 0.85 g/cm^3, followed by a 50-mg/cm^3 carbon resorcinol formaldehyde (CRF) foam reservoir. The hohlraum was driven using 12 beams with a 1-ns square pulse to produce a peak radiation temperature of 200 eV. The resulting blast wave caused the metallic foam/reservoir interface to become unstable, resulting in Rayleigh–Taylor (RT) instability growth. The shock tube was imaged using a point-projection backlighter technique with a 10-μm-diam Ag wire on a polystyrene substrate and illuminated with an OMEGA EP short-pulse beam. The interface mix was characterized by 90%–10% transmission contour between the CRF/sample interface. Figure 14(a) shows a typical radiograph obtained during the experiment. The interface position was estimated using the Au washer around the shock tube [seen as the dark band on the bottom of Fig. 14(a)] and the position of the steepest gradient at the interface. Due to complications on the shot day, only two data points were obtained with data at 18 ns and 21 ns from the start of the OMEGA laser drive. The data were combined with the previous

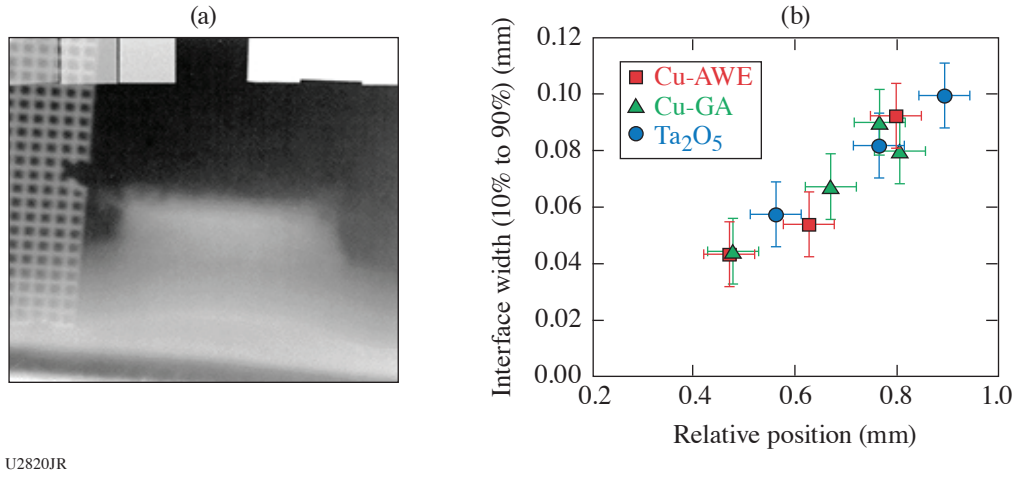

Figure 14
(a) Background subtracted radiography of Ta_2O_5 foam (shot 99129) at 21 ns; (b) measured mix width as a function of interface position extracted from the radiographs. AWE: Atomic Weapons Establishment; GA: General Atomics.

Ta_2O_5 data on FoamGrw 19A at 23.5 ns and agree with the suggested trend [Fig. 14(b)]. Additionally, the Ta_2O_5 mix width from Ta_2O_5 also agrees with the Cu-foam data, suggesting there is no significant difference between the two foams with regard to the mix width. Further studies are looking at the role of decompression, which can mask the role of internal structure on mix width.

Interaction Between a Strong Laser Ablation Shock and a Shock Wave from the Supersonic-to-Subsonic Transition of Radiation
Principal Investigator: D. Rusby (LLNL)
Co-investigators: F. Albert, K. Widmann, C. Harris, A. Toreja, S. Murray, and S. Prisbrey (LLNL); and H. G. Rinderknecht (LLE)

Radiation transport plays an important role in many areas, such as ICF experiments, energy transport in the sun, or the penetration of the radiation field from a hot star or supernova interacting with an interstellar cloud. The ESPADA platform was designed to observe the shock front induced by the supersonic-to-subsonic transition of a Marshak wave (a radiation flow propagating into a medium) in silica aerogel and compare the results with the radiation-hydrodynamic code *KULL*. Supersonic-to-subsonic radiation transition induces a diagnosable shock wave that can be observed with x-ray radiography but has seldom been investigated in experiments.[15] We successfully observed and measured this transition during our ESPADA-20A shot day. In 2021, we did two additional shot days (ESPADA-20B and ESPADA-21A) to observe the collision of the Marshak-induced shock wave with a strong (few-Mbar) laser ablation shock. Within this context, the strong shock is an effective and reliable probe of the Marshak-induced shock wave behavior, and the shock interactions provide a test of our ability to model the behavior of materials in a complex physical regime.

During the ESPADA-20B/21A shot days, a halfraum was driven to temperatures of ~100 eV by 21 OMEGA beams (3-ns flattop pulse shape with 273 J/beam). This x-ray drive launched a Marshak wave through a 2-mm-diam, 2-mm-long, 30-μm-thick gold tube filled with SiO_2 foam (33 mg/cm^3) and attached on the other side of the halfraum. On the other side of the foam tube, a strong laser ablation shock was driven with six beams (same pulse shape and energy, 2.5 to 3 ns earlier) incident onto either a 10-μm CH or 2-μm Al ablator. A 12-μm-thick Ti foil was driven with 23 additional beams to provide a near-monochromatic 4.7-keV x-ray backlighter source oriented quasi-perpendicular to the gold tube's axis. A 200-μm-wide slit on each side of the tube allowed the x rays to pass through the foam, and the x-ray images of the target were recorded on a four-strip x-ray framing camera, at different times (Fig. 15).

Our initial results show reasonable agreement between the experiment and 2-D *KULL* simulations.[16] Detailed simulations are underway for a post-shot comparison. Our next experiments (ESPADA 22) will use Ni-doped foams and Fresnel zone plates for increased spatial resolution.

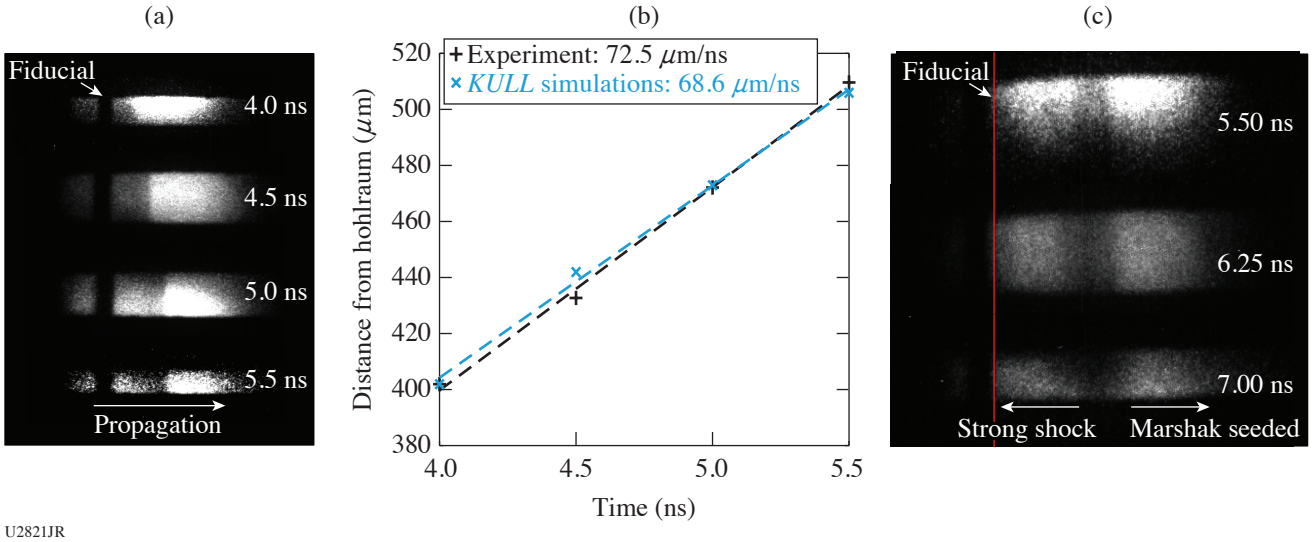

Figure 15
Experimental data showing the (a) Marshak wave-induced shock and (c) its propagation after collision with a strong laser-ablation shock. (b) The experimental shock velocity is well reproduced by 2-D *KULL* simulations.

X-Ray Sources from Laser Wakefield Acceleration on OMEGA EP

Principal Investigator: F. Albert (LLNL)

Co-investigators: I. Pagano (LLNL and the University of Texas, Austin); N. Lemos, J. Williams, and H. Chen (LLNL); J. L. Shaw and D. H. Froula (LLE); A. Aghedo (Florida A&M University); and M. Sinclair and C. Joshi (University of California, Los Angeles)

X-ray backlighting is one of the most commonly used methods to look into the extreme temperatures, pressures, and densities created during laser-driven HED science experiments. Over the years, much effort has gone into developing backlighting techniques to look into these states of matter using new sources and diagnostics. The properties of an x-ray backlighter (flux, source size, spectrum, duration) required for an experiment depend on the application being studied and on the quantity being measured. The goal of the Wakefield-EP shot series is to develop a new type of x-ray backlighter, which could be advantageous for applications requiring broadband spectra, small source sizes (sub-50 μm), short-duration (less than 10 ps), and x rays extending beyond 100 keV. Our proposed x-ray sources are based on laser wakefield acceleration (LWFA) of electrons in the self-modulated regime (SMLWFA). Specifically, we aim to develop three different x-ray sources based on betatron radiation, Compton scattering, and bremsstrahlung emission.

The Wakefield-EP-21A and Wakefield-EP-LBS-21A shot days were a continuation of our previous work, aimed at producing and detecting betatron radiation produced by SMLWFA using a modified version of the electron–positron–proton spectrometer (EPPS) diagnostic. We enlarged apertures to 5 mm (instead of 1 mm) and included a hole at the back of the magnet box, as well as a stack of nine image plates at the back of the ten-inch manipulator (TIM) boat to detect betatron radiation. With the help of Monte Carlo simulations, we implemented diagnostic shielding enhancements for our 2021 shot days. As a result, we were able, for the first time, to simultaneously detect electrons and betatron x rays in our OMEGA EP experiments (Fig. 16).

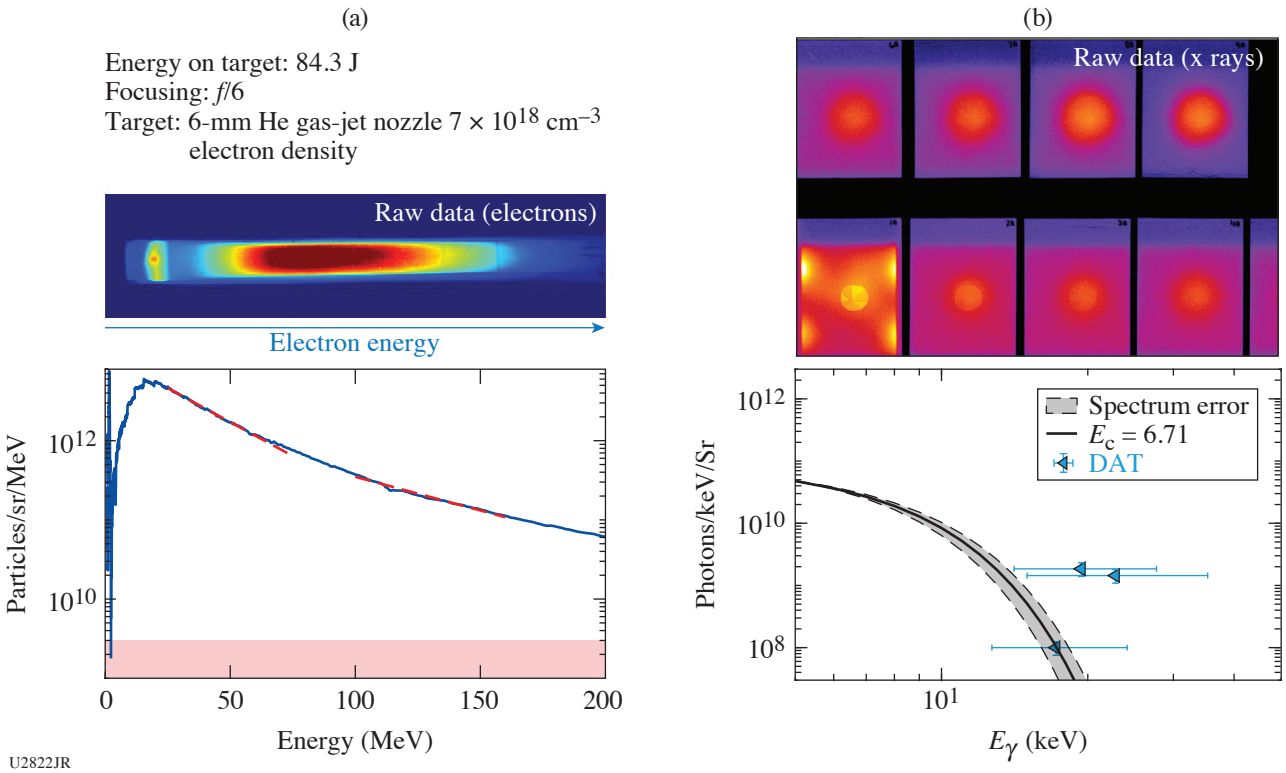

Figure 16

Results obtained during the WakefieldLBS-EP-21A shot day using the modified EPPS diagnostic. (a) Electron data; (b) betatron x-ray signal measured on the rear image plate stack of EPPS with reconstructed spectrum.

The wakefield platform produced robust electron beam data, recording >100-nC charge electron beam at each shot, as well as two temperature spectra extending up to about 200 MeV [Fig. 16(a)]. We also measured betatron x rays with critical energies between 5 to 10 keV and 10^{10} photons/keV/sr [Fig. 16(b)].

The Measure of X-Ray Emission from Laser-Compressed Spheres
Principal Investigator: E. V. Marley
Co-investigators: M. Tabak, K. Widmann, and J. Emig

This campaign, conducted to measure the x-ray emission from laser-compressed spheres, was the first campaign in the development of a new experimental platform. The target was a gas-filled, 800-μm-diam plastic sphere illuminated by 60 beams with a 1-ns square pulse. Five framing cameras and one streak camera were used to record the x-ray emission. Two of the framing cameras were coupled to pinhole cameras to measure the size of the emitting volume. The remaining three framing cameras were coupled to spectrometers to record various bands of the x-ray emission of the compressed sphere (Fig. 17). The time-resolved emission was also recorded with Dante. The Henway spectrometer was also fielded to record the absolute, time-integrated emission of the compressed spheres. Eleven shots were completed successfully with data being collected on all eight diagnostics.

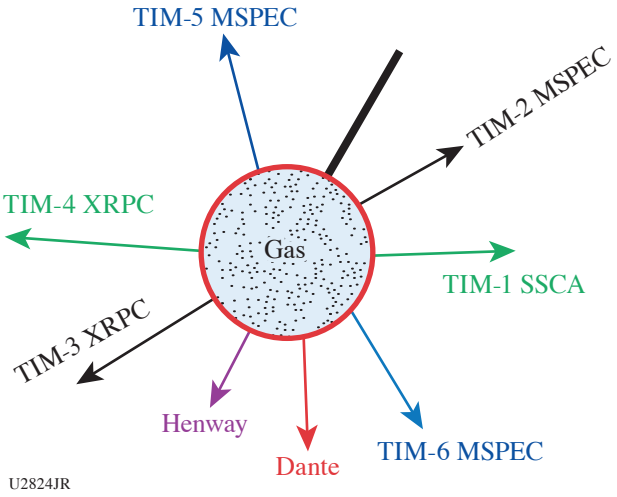

Figure 17
Experimental configuration of the XELCS. MSPEC: multipurpose x-ray specrometer; XRPHC: x-ray pinhole camera; SSCA: static spherical cavity approximation.

Probing Buried-Layer Nuclear-Heated Samples
Principal Investigator: A. B. Zylstra
Co-investigator: J. Burggraf

There is significant interest in conducting nuclear physics experiments with target nuclei in a HED plasma environment. This is because under conditions typical for our experimental facilities, some nuclei can have excited states populated by interaction with the plasma. These processes are intrinsically interesting in themselves, and the subsequent impact of the excited states on nuclear physics is unknown. For example, in the r process of heavy-element nucleosynthesis, sequential neutron capture occurs on heavy elements under extreme conditions and such physics is often incorporated into “stellar enhancement factors” on the cross sections, which are purely theoretical.

To study this physics in the lab, we require a mechanism to heat samples to relevant conditions and then probe nuclear reactions with a source of particles. This campaign is designed to study the heating, starting with the buried-layer heating mechanism. Unlike previous applications of this heating technique, studying nuclear physics will require substantially larger sample masses for measurable signals. To this end, we began by performing a scaling experiment on OMEGA EP at the end of FY21 using buried Cu layers and x-ray spectroscopy.

The experimental configuration is shown in Fig. 18. Several spectrometers were used to measure Cu emission on each shot, with variables including laser energy, pulse duration, and buried Cu layer thickness scanned over the data. Data analysis is in progress.

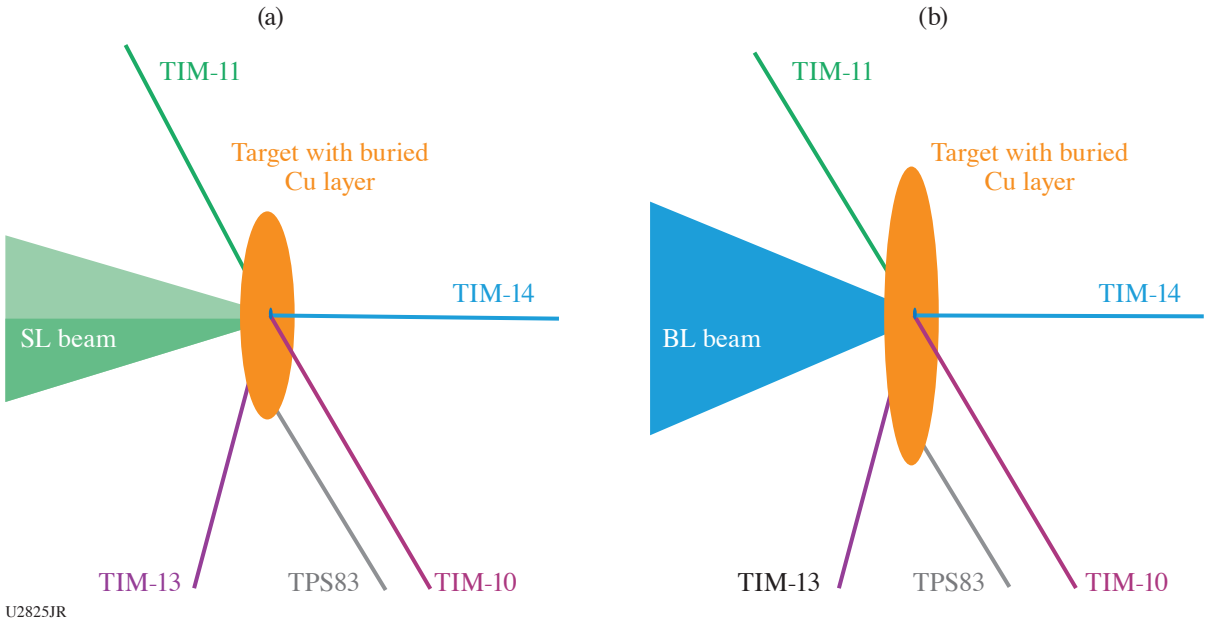

Figure 18
VisRad drawings of the experimental configuration for NucHeat-21A, which used alternating sidelighter (SL) and backlighter (BL) shots to increase data return.

Materials Campaigns

OMEGA-60 and OMEGA EP Experiments on Laser-Driven Tin Ejecta Microjet Interactions
Principal Investigator: A. M. Saunders (LLNL)
Co-investigators: C. V. Stan, K. K. Mackay, B. Morgan, J. Horwitz, S. J. Ali, T. Haxhimali, Y. Ping, F. Najjar, J. H. Eggert, and H.-S. Park (LLNL); and H. G. Rinderknecht (LLE)

The ejecta campaign on OMEGA 60 and OMEGA EP seek to understand the effects of ejecta microjet interactions from laser-driven tin targets through x-ray radiography measurements. An ejecta microjet forms when a shock breaks out from a free surface and interacts with a surface feature, such as a groove carved across the sample. The interaction of the shock with the free surface causes the surface feature to invert as a limiting case of the Richtmyer–Meshkov instability, and the groove turns into a planar jet of material propagating at velocities in excess of several kilometers per second. Micron-scale particles comprise ejecta microjets, and as such, the interaction of two ejecta microjets offers an experimental methodology for anyone interested in the collisions of high-velocity particle-laden flows.

Figure 19(a) shows a schematic of the radiography platform on OMEGA EP. Two long-pulse lasers drive shock waves into tin samples oriented toward each other. The inside surfaces of the tin foils have grooves carved across them. The shock waves generate planar microjets traveling toward each other, eventually to interact at the center of the two foils. At a later time, a short-pulse laser is incident on a titanium microwire, generating x rays to be used for radiography and captured by an image plate held in the shielded image-plate diagnostic. Figure 19(b) shows a picture of the target, and Fig. 19(c) shows the dimensions of the target and the groove, as well as radiation-hydrodynamic simulations of one shock wave propagating through a tin sample. The platform on OMEGA-60 is similarly built, with the geometry designed such that the jets interact with a 170° angle between them; a long-pulse laser on a pinhole backlighter is used to generate the x rays for the radiography measurement.

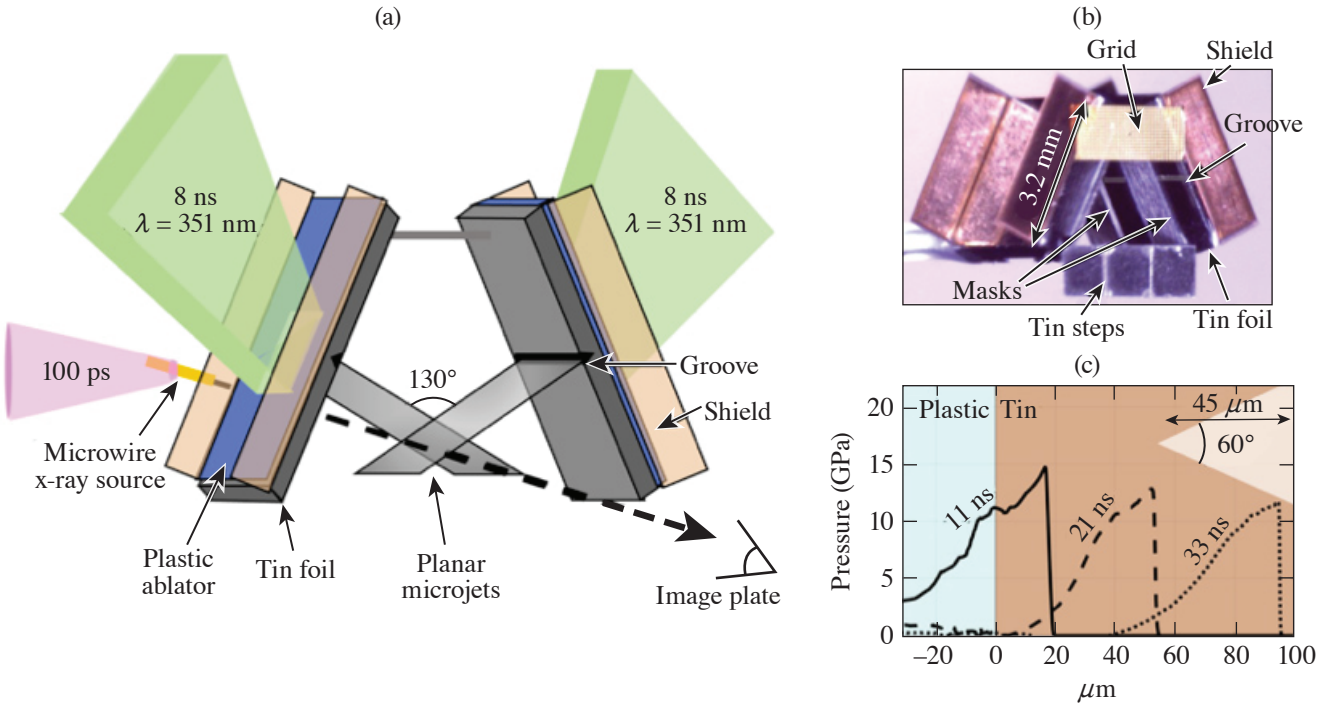

Figure 19
(a) A schematic of the platform on the OMEGA EP laser. Two long-pulse lasers drive shock waves into tin foil targets with grooves imprinted on their inner surfaces. The interactions of the shock waves with the grooves generate planar ejecta microjets that interact. A short-pulse laser incident on a microwire generates x rays for the radiography measurement. (b) A photo of the target. (c) Target thicknesses and groove dimensions with radiation-hydrodynamic simulations of a shock wave propagating through a tin sample.

Both the OMEGA-60 and OMEGA EP platforms were very successful in collecting radiography data on interacting ejecta microjets. Figure 20 shows examples of data collected from (a) the OMEGA EP and (b) the OMEGA-60 platforms. For experiments on OMEGA EP, we varied the laser drive energy such that we interacted jets at drive pressures ranging from 11.7 GPa to 116.0 GPa. The first two columns of Fig. 20(a) show images of jets at those high and low pressures before interaction (top row) and after interaction (bottom row). We observe that at the lower pressures, the jets appear not to interact, while at higher pressures, the jets interact strongly and form a corona of material around the center point. We also took data of interacting jets at an intermediate pressure, as seen in the right column of Fig. 20(a). These data occurred with a differently shaped grove, which resulted in the altered jet shape. No interactions were observed at this intermediate pressure. The results from the OMEGA EP platform were featured in a recently accepted article in Physical Review Letters.[17]

We wanted to understand the drive pressure at which interaction onset behavior changed, so we used the platform on OMEGA-60 to perform a finer pressure scan of head-on interacting jets. The data from this campaign can be seen in Fig. 20(b), where interaction images were taken at 74, 103, and 116 GPa. It appears like interaction behavior does not become apparent until pressures exceeding 103 GPa are reached. This is significant because tin is a material known to melt upon shock release at pressures exceeding approximately 50 GPa. If the interaction behavior changed as a function of tin material phase, we would expect to see a change at shock pressures around 50 GPa. However, because we see a change at higher pressures, this suggests that interaction behavior is driven by other jet characteristic, such as jet density, particle-size distribution, or jet velocity. Understanding the physics driving microjet collisions will be the study of future campaigns.

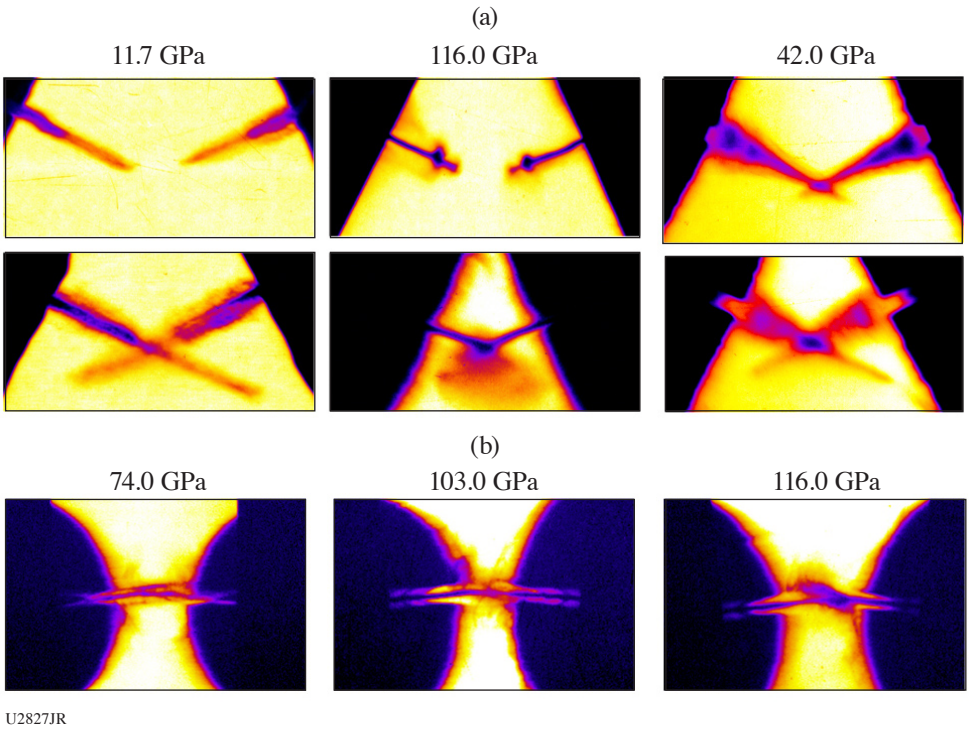

Figure 20
X-ray radiography images of laser-driven tin ejecta microjets and their interaction behavior observed in (a) OMEGA EP experiments and (b) OMEGA-60 experiments at various driver pressures.

Measuring the Hugoniot of Shocked LLM-105
Principal Investigator: S. M. Clarke (LLNL)
Co-investigators: M. C. Marshall (LLE); and J. H. Eggert, R. Smith, L. Leininger, and L. Fried (LLNL)

Generating high-quality experimental EOS data of insensitive high explosives (HE's) such as TATB and LLM-105 is essential to improving predictive modeling of the behavior of these materials. Previous work demonstrated the feasibility of using OMEGA EP to obtain EOS data on TATB.[18] This research led to a better understanding of the overdriven state [pressures exceeding the Chapman–Jouguet (CJ) pressure] that would not have been achievable using standard gas-gun or explosive-driven techniques.

This campaign measured the shock Hugoniot of an LLM-105 formulation using the impedance-matching technique relative to an aluminum standard (Fig. 21). HE samples were created by pressing parts and polishing them down to the thinnest-possible dimension. They were attached to an Al pusher, which was driven by a CH ablator [Fig. 21(b)]. A LiF witness was used to infer the time dependence of the shock velocity in the adjacent opaque HE sample to obtain a more-accurate Hugoniot measurement than that using the average shock velocity determined from the shock transit time. Since the HE samples were relatively thick (~200 μm), all four OMEGA EP beams were stitched together to obtain an ~40-ns pulse [Fig. 21(c)] to support a nearly steady shock. For pressures under ~55 GPa, excellent reflectivity was observed at the Al/LiF witness interface [Fig. 21(d)], enabling us to extract particle velocity as a function of time using VISAR [Fig. 21(e)].

Preliminary analysis of the data using the average shock velocity in the HE sample suggests we are achieving higher densities than what was predicted by the unreacted Hugoniot [Fig. 21(f)]. Future analysis will focus on using the nonsteady waves approximation to get a better pressure determination in the HE samples based on our knowledge of the shock velocity history in

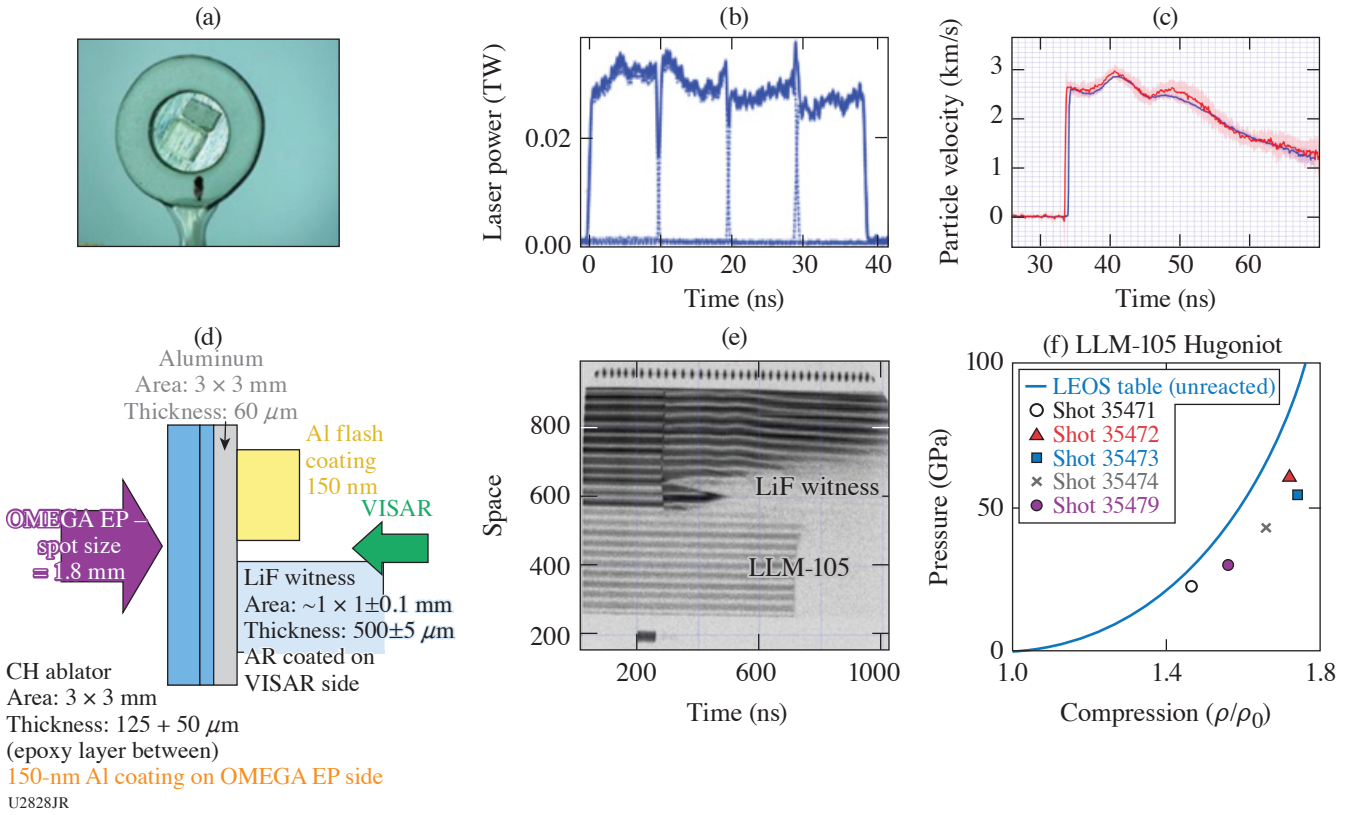

Figure 21
(a) Optical image of the as-shot target package. (b) Schematic of the target package detailing the position of the HE sample relative to the LiF witness. (c) Typical delivered pulse shape consisting of all four beams of OMEGA EP stitched together to create an ~40-ns drive. (d) Typical active shock breakout (ASBO) data achieved during the shot showing excellent reflectivity at the Al/LiF witness interface and the shock breakouts of the aluminum baseplate and the LLM-105 formulated sample. (e) Al/LiF interface velocity versus time. (f) Preliminary plot of the data obtained during this campaign compared to the LEOS table for unreacted LLM-105.

the LiF witness. The next campaign will focus on extending the range of data from 15 GPa to 80 GPa and filling in more data points around the CJ pressure.

Generating Very Low-Pressure Shocks Using Alternative Ablator Materials

Principal Investigator: R. Smith

The purpose of this campaign is to evaluate alternative ablator materials for use in future low-pressure (1) shock-compression experiments (Be, Cu, Al, Ag) and (2) ramp-compression experiments (diamond). While Kapton® (polyimide) has been a widely used ablator material in laser-compression experiments, the use of this material is complicated by a proposed phase transformation at ~20 to 50 GPa, which can result in an unstable compression wave being formed (multiwave structure). Therefore, there is a need for alternative ablator materials that can transmit shock waves without additional compression-wave pulse shaping due to the deformation processes in the ablator material itself. In this study each target consisted of a 25-μm-thick ablator (for shock experiments) or a 100-μm-thick diamond ablator (for ramp experiments). These ablator materials were glued onto to a 0.2-μm Al-coated LiF window. The phase plate used in these experiments produced a 1.8-mm-diam laser spot on target, and the laser pulse shaping requested for each ablator material is shown in Fig. 22. The primary diagnostic was the EP-ASBO system (VISAR) that recorded the ablator-LiF particle velocity as a function of time. For all ten shots, the laser pulse shaping was excellent and high-quality data were obtained.

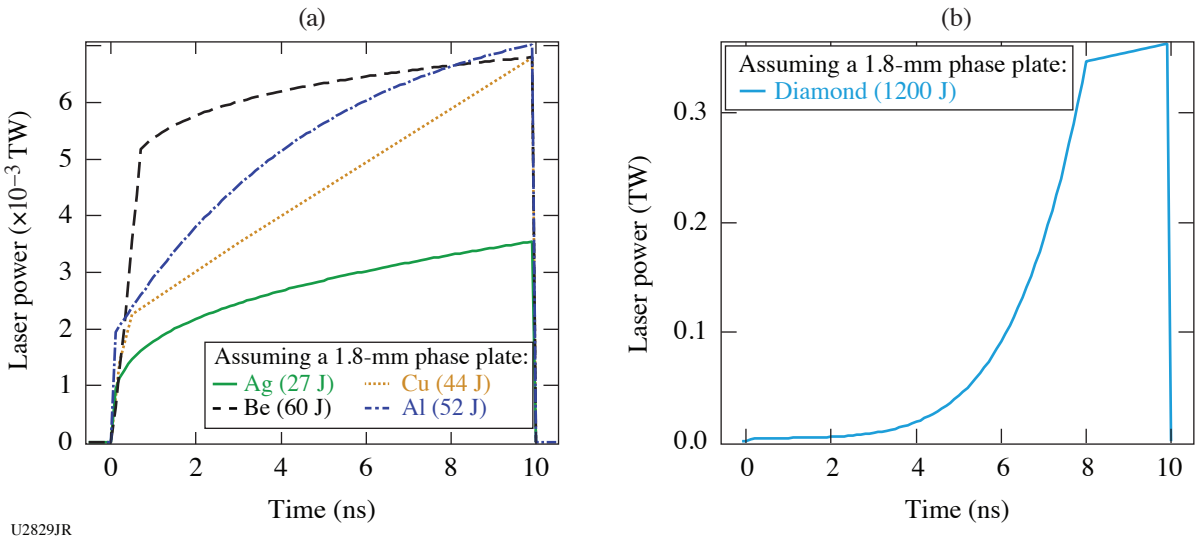

Figure 22
Laser pulse shape for (a) temporally steady-shock experiments through different ablator materials and (b) ramp-compression experiments.

Improving Reflection Diffraction Signal for the Forward–Backward X-Ray Diffraction Diagnostic
Principal Investigator: A. Krygier (LLNL)
Co-investigators: D. N. Polsin, M. K. Ginanne, and J. R. Rygg (LLE); and C. E. Wehrenberg and J. H. Eggert (LLNL)

We are developing a new platform to simultaneously measure transmission and reflection x-ray diffraction from a dynamically compressed sample. The goal of this platform is to determine the strain anisotropy induced in a sample due to material and flow strength. This platform is related to the PXRDIP diagnostic but has unique challenges due to the need for multiple simultaneous backlighters.

In the XRDAFS-20A experiment, we were attempting to improve the reflection diffraction signal by improving backlighter alignment and reduce background sources. In preparing the instrument, we were able to identify a systematic alignment issue during the build that we corrected with a careful procedure. We also fielded metallic glass (diffractionless) shields on the pinhole to mitigate non-sample diffraction, which was found to work well. Three of the shots fielded undriven samples to test iterations in the configuration; the remaining two shots were driven, one of which was reflection backlighter only and the second of which attempted simultaneous reflection and transmission diffraction. The driven reflection measurement (Fig. 23) showed clear driven diffraction from iron—the first recorded reflection diffraction from a high-pressure sample on this platform. The second driven shot showed transmission diffraction, but not reflection, indicating continuing alignment issues to be addressed in experiments to come.

Transmission and Reflection Diffraction of Fe Using the FBXRD Diagnostic
Principal Investigator: A. Krygier (LLNL)
Co-investigators: D. N. Polsin, M. K. Ginanne, and J. R. Rygg (LLE); and C. E. Wehrenberg and J. H. Eggert (LLNL)

We are developing a new platform to simultaneously measure transmission and reflection x-ray diffraction from a dynamically compressed sample. The goal of this platform is to determine the strain anisotropy induced in a sample due to material and flow strength. This platform is related to the PXRDIP diagnostic but has unique challenges due to the need for multiple simultaneous backlighters.

In the FBDiff-21A experiment, we were using the advances made on previous experiments to attempt to collect simultaneous transmission and reflection diffraction from shock-compressed iron. We varied the pinhole size and collimator diameter to scan

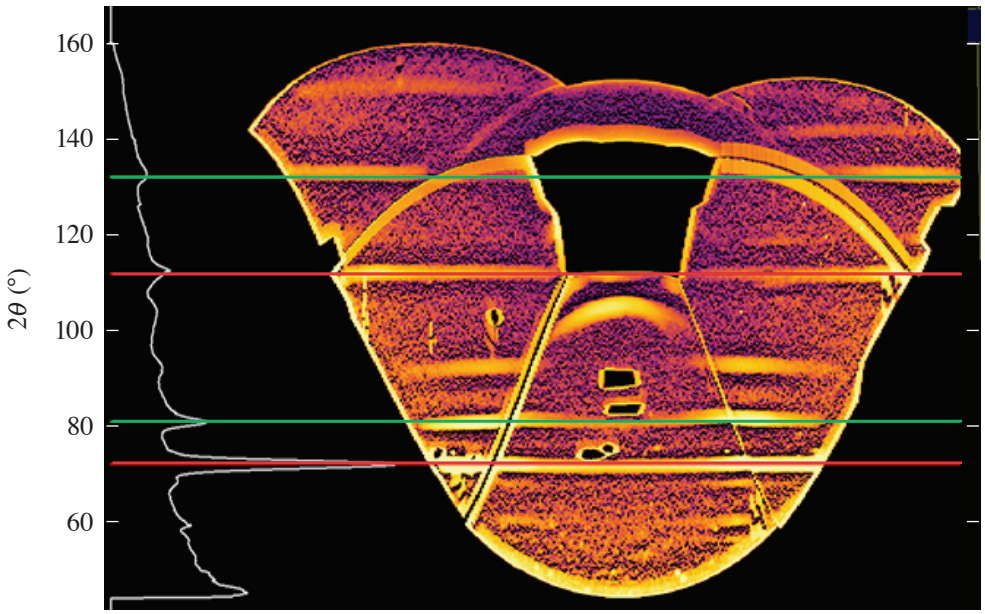

Figure 23
Background subtracted forward–backward x-ray diffraction (FBXRD) data in a reflection-only configuration, projected in polar-azimuthal coordinates. The red and green lines identify the expected location of diffraction from the W pinhole (red) and the Fe sample (green). Driven features are present at $2\theta \sim 90°$.

different balances of expected diffraction quality (higher with smaller pinhole and collimator) and expected signal (higher with larger pinhole and collimator). We successfully observed simultaneously driven transmission diffraction and ambient reflection diffraction on more than one shot. There is still a significant amount of unwanted signal and apparent backlighter/collimator/sample alignment issues that will be the subject of future experiments (Fig. 24).

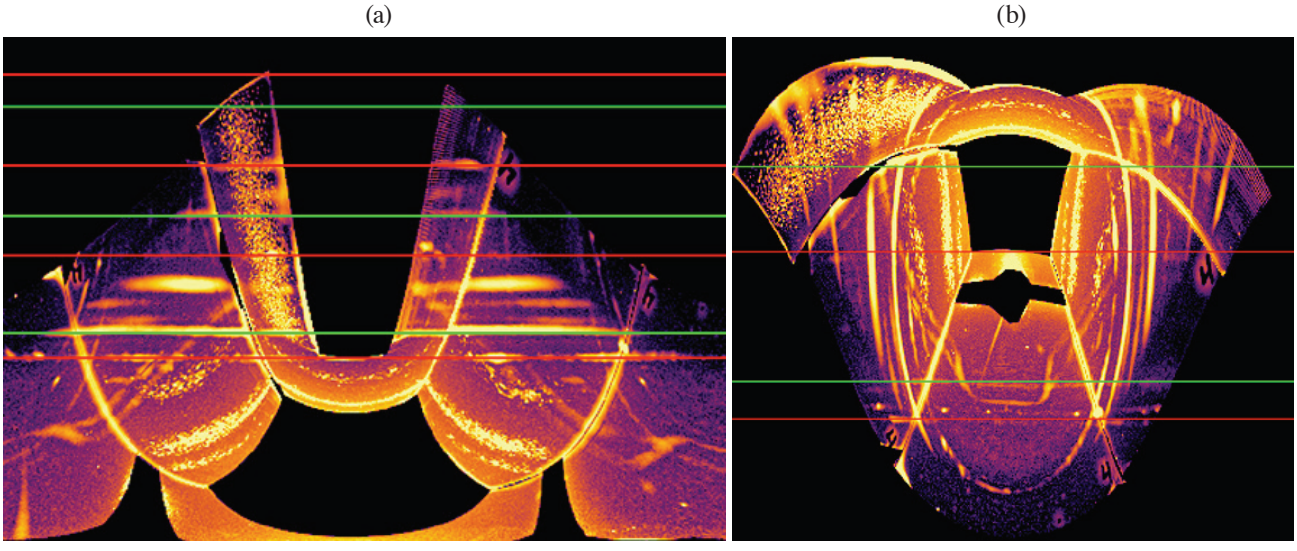

Figure 24
Background subtracted FBXRD data in transmission and reflection. The data are shown projected in polar–azimuthal coordinates with respect to each backlighter; (a) transmission geometry and (b) reflection. The red and green lines identify the expected location of diffraction from the W pinhole (red) and the Fe sample (green). Unmarked lines in the transmission data correspond to the high-pressure hcp phase of iron.

Off-Hugoniot Study of the Phase Behavior of Shock-Ramp–Compressed Au

Principal Investigator: A. L. Coleman

Co-investigators: R. F. Smith, T. E. Lockard, D. C. Swift, and J. McNaney

Gold is widely used throughout the high-pressure community; in static compression, it is a commonly used pressure standard for diamond-anvil cell experiments[19] as well as being used as a heat shield in dynamic compression target packages on the NIF and OMEGA.[20] While there has been much study of the structural behavior of Au at room temperature,[21,22] its behavior at high pressures *and* high temperatures is not well constrained. When Au is used as a component in shock- and ramp-compression target packages, it is important that its structural behavior is well understood so that any contribution it makes to a diffraction data set may be confidently identified.

We have designed a series of shock-/ramp-compression shots to explore Au across a series of different temperature states. This was achieved by initially shocking the sample to an on-Hugoniot state and then ramp compressing to a final pressure state, where the sample was probed by x-ray diffraction to determine the crystallographic state. Figure 25(a) shows the designed initial shock (red) and final ramp (green) compressions, with initial shock states at 50, 100, 150, and 200 GPa. Also shown on this plot are predicted phase boundaries from Smirnov,[23] as well as previously obtained Au data from shock[24] and ramp[25] compression.

By using a multilayered target package and a series of individually designed laser drives, we were able to obtain high-quality diffraction data between 350 and 650 GPa; example raw and integrated data are shown in Figs. 25(b) and 25(c), respectively. VISAR was employed as a secondary diagnostic in the campaign to allow pressure determination. Over two shot days, we took 16 shots and successfully characterized the structural behavior of Au at several different pressure and temperature states.

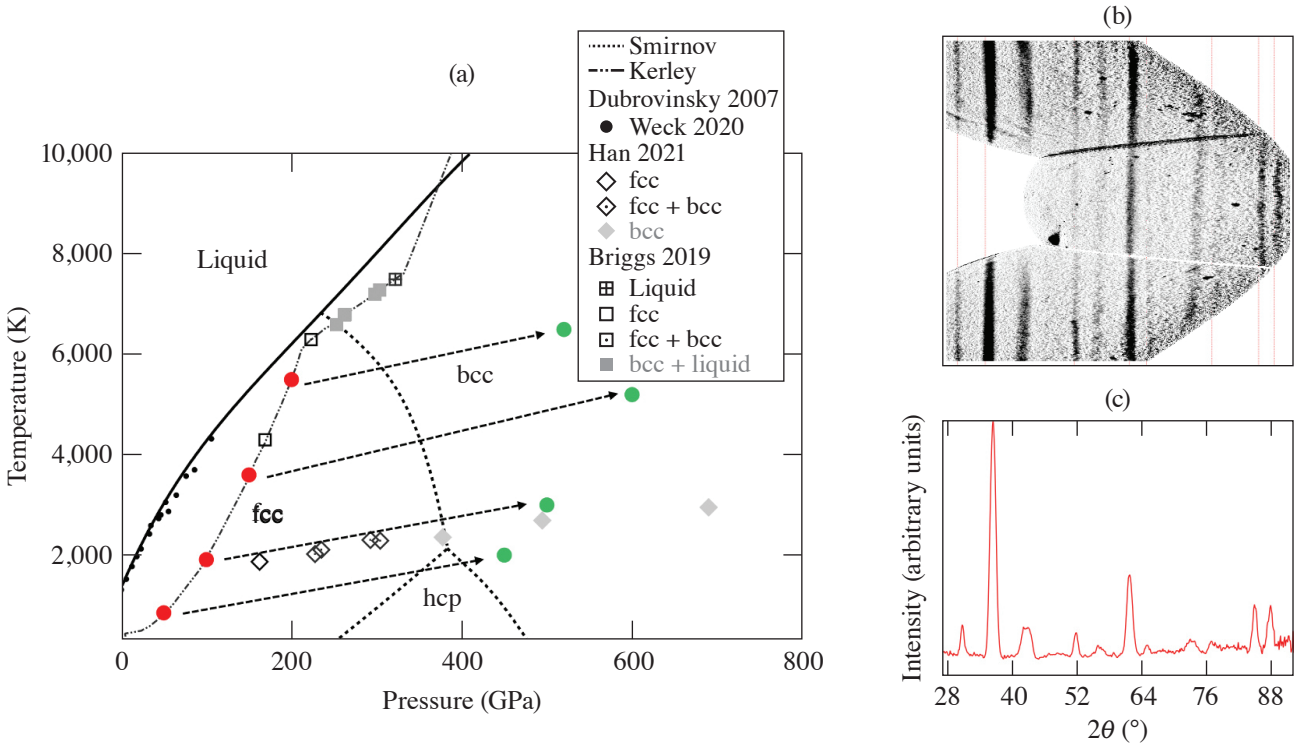

Figure 25

(a) The phase diagram of Au with theoretically predicted phase boundaries and data from previous studies is shown. The shock- and ramp-compression states are shown by red and green points, respectively. (b) Raw and (c) integrated data from the Au target package are shown.

EXAFS Measurements of Shock Compressed Fe Using the IXTS Spectrometer for Temperature Determination

Principal Investigator: A. L. Coleman
Co-investigators: F. Coppari, Y. Ping, and J. McNaney

Temperature determination is a significant challenge in modern laser-driven, dynamic compression experiments. The nanosecond time scales and extreme pressure and temperature conditions at which these experiments are conducted mean that the successful implementation of a temperature diagnostic is challenging and frequently not possible. A potential means of obtaining temperature information about a shock- or ramp-compressed sample lies in the analysis of EXAFS (extended x-ray absorption fine structure) data. As a material becomes hotter, thermal motion of the atoms becomes important and reduces the amplitude of the EXAFS oscillations in a manner that is proportional to the temperature increase.

The purpose of this campaign was to optimize the imaging x-ray Thomson spectrometer (IXTS)[26] [Fig. 26(a)] in order to obtain high-quality EXAFS data from Fe at a series of shock-compressed states with the intention of determining the sample's temperature through the analysis of the EXAFS spectra. In addition to running the IXTS as the primary diagnostic, VISAR data were also obtained to establish the pressure in the Fe sample. Over the course of the two half-day campaigns, 12 shots were taken. Shock-compressed and ambient data sets were obtained along with a flat-field shot (taken once every campaign), which was used to correct the effects of the IXTS crystal defects on the EXAFS data. This experimental configuration made use of a Ti foil backlighter x-ray source, driven by 8 kJ in a 1-ns laser pulse.[27] The main target, consisting of a Kapton® ablator, an iron foil, a Cu temper layer, and a LiF window (Cu being closely impedance matched to Fe allowed us to hold a steady shock-pressure state in the Fe layer for the entire 1-ns duration of the backlighter x-ray source).

During these campaigns we successfully determined that heating the sample from the backlighter source is of the order of ~300 K [Fig. 26(b)] by comparing data from an undriven target with FEFF calculations for Fe at different temperatures. We also established that the resolution of this experimental setup is ~8 eV. We collected EXAFS data from the Fe shock compressed up until melting and observed a reduction in the amplitude of EXAFS oscillation in targets that were shock compressed to higher temperatures [Fig. 26(c)]. Analysis is ongoing to implement flat-field correction and determine temperature from the measured EXAFS data.

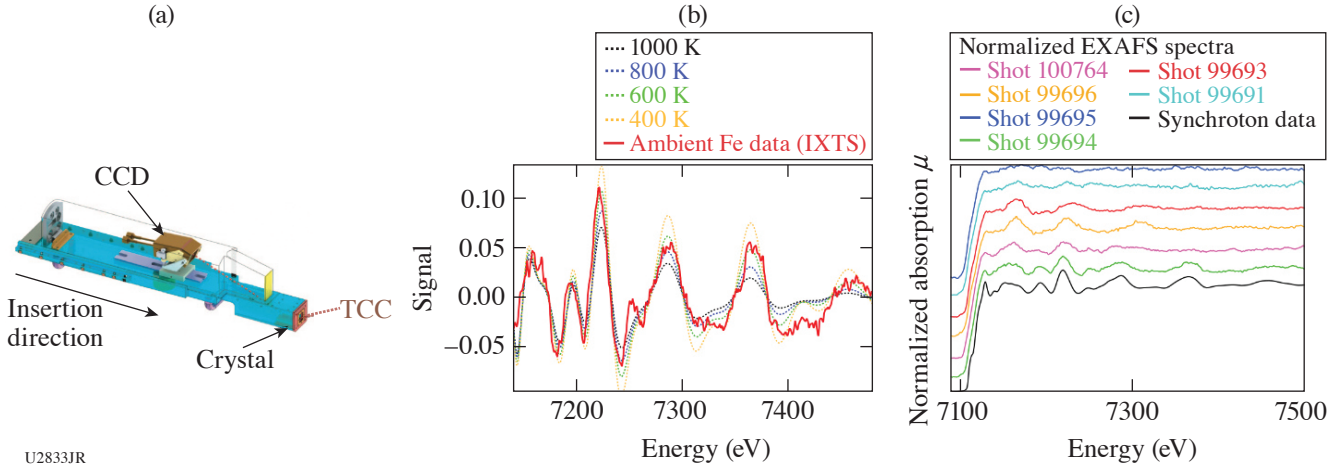

Figure 26
(a) The IXTS spectrometer schematic.[26] For our experiments, a curved Ge(220) crystal was used to disperse x rays in the energy range around the Fe absorption edge (7.1 keV). (b) EXAFS signal from an undriven Fe target is shown in red, along with simulated data from FEFF for different temperatures at ambient pressure (c) Ambient synchrotron data (black), ambient IXTS data (green), and shock-compressed data at increasing pressure and temperature are shown. As the temperature increases, the EXAFS oscillations decrease in amplitude due to Fe thermal motion. CCD: Charge-coupled device; TCC target chamber center.

Tin and Epoxy Strength Exploration Using the Rayleigh–Taylor Instability

Principal Investigator: C. V. Stan (LLNL)

Co-investigators: H.-S. Park, T. Lockard, D. Swift, and J. McNaney (LLNL); M. P. Hill (AWE); and G. Righi (University of California, San Diego)

We measure plastic deformation in tin using directly driven targets with machined sinusoidal perturbations, taking advantage of the RT instability. The targets consist of a Be ablator (20 μm), a brominated plastic layer (20 μm), epoxy (5 to 7 μm), rippled tin (40 μm), a LiF window (500 μm), and calibration features. Radiography data were collected at varying time points (20 to 50 ns from laser start time) using a microwire or microflag backlighter and a short-pulse beam to determine ripple growth. Prior work has shown that the growth of tin under these conditions (~1 Mbar, ~K) was unusually and systematically low, pointing to possible extremely high strength in this material, which we were unable to match with conventional models.

One hypothesis is that the growth in tin may be suppressed by the possible strength in other target components, namely the brominated plastic or epoxy layers. To test this, we compressed tin targets to similar pressure conditions (~1 Mbar), but higher temperature (~7000 K), in order to induce melting. Deviations from the predicted ripple growth may then point to the effect of strength in plastic components on the RT growth within the system.

One VISAR and three radiography measurements were collected. The VISAR shows one strong initial shock to ~3 km/s, followed by two more, smaller shocks, at ~10 and ~20 ns (Fig. 27). These correspond to the beam stitching times and may indicate that our individual beam pulse shapes or overlap times need adjustment going forward. The three radiographs show slightly low RT growth when compared to the models, although still just within the experimental error; further data analysis is needed. One interesting observation was that when a wire backlighter was used (30-ns data point), the data from different ripple amplitudes appeared more self-consistent, with a flatter background overall, than when a microflag backlighter was used (25- and 27.5-ns data points). A long-pulse backlighter will be implemented on future shots to investigate systematics associated with the choice of x-ray source.

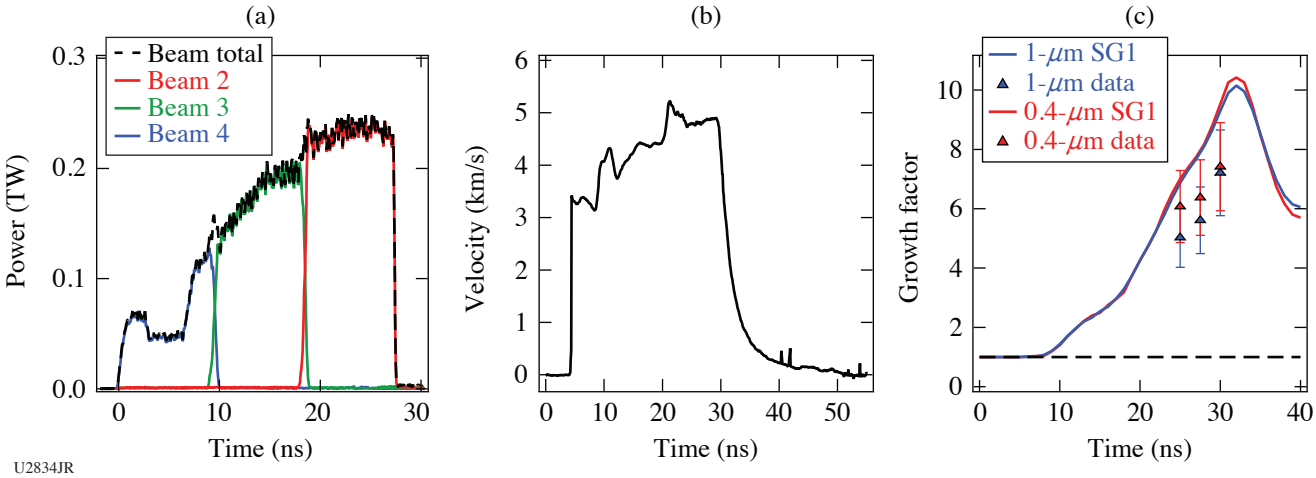

Figure 27

(a) Power delivery from three UV beams for one of the data shots. The total beam power is depicted by the dotted line. Power delivery closely matches the requested level. (b) VISAR Leg A data, showing shocks corresponding to power blips at beam stitching times. (c) RT growth calculated at three different data-collection times. The growth appears somewhat lower (but perhaps within error) of the predicted values.

Rayleigh–Taylor Strength Measurements of Copper Versus Epoxy

Principal Investigator: C. V. Stan (LLNL)

Co-investigators: H.-S. Park, T. Lockard, D. Swift, and J. McNaney (LLNL); M. P. Hill (AWE); and G. Righi (University of California, San Diego)

The effects of epoxy or other plastics on the RT growth of instabilities at temperatures relevant to solid metals (≲8000 K) and pressures around 1 to 2 Mbar have not been previously quantified. We have taken several measurements of directly driven tin targets with sinusoidal perturbations, where the perturbation growth was lower than can be explained by reasonable strength models. In this project we replaced tin with copper in order to provide additional benchmarking of the behavior of plastic-containing targets. The targets consisted of a Be ablator (20 μm), a brominated plastic layer (20 μm), epoxy (5 to 7 μm), rippled Cu (40 μm), a LiF window (500 μm), and fiducials. Ripple growth as a function of pressure/temperature variation was determined by face-on radiography, collected at 25 and 30 ns from laser start time using a microflag backlighter irradiated by a short-pulse beam (Fig. 28). The RT unstable interface was driven to two different temperature conditions using ramped drives with higher or lower initial shocks.

One VISAR and four radiography measurements were collected. Only the low-temperature drive was collected in VISAR due to instrumentation failure during the shot day; the results confirm that a smooth ramp with no stitching errors was produced. The four radiographs show somewhat poor contrast, which may be due to the choice of backlighter material (Cu) or the hard x-ray background from the high-intensity, short-pulse interaction with the foil. In the future, a long-pulse backlighter will be used to reduce this bremsstrahlung contribution. Preliminary analysis using only the fiducial ripples indicates that the growth is comparable to the models, suggesting that the epoxy layer may not be the cause of previously observed low growth rates in tin. The error bars are large enough at this early stage, however, to warrant caution in drawing firm conclusions. Future shots will focus on (1) determining the repeatability of the stitched drive via additional VISAR measurements and (2) comparing additional

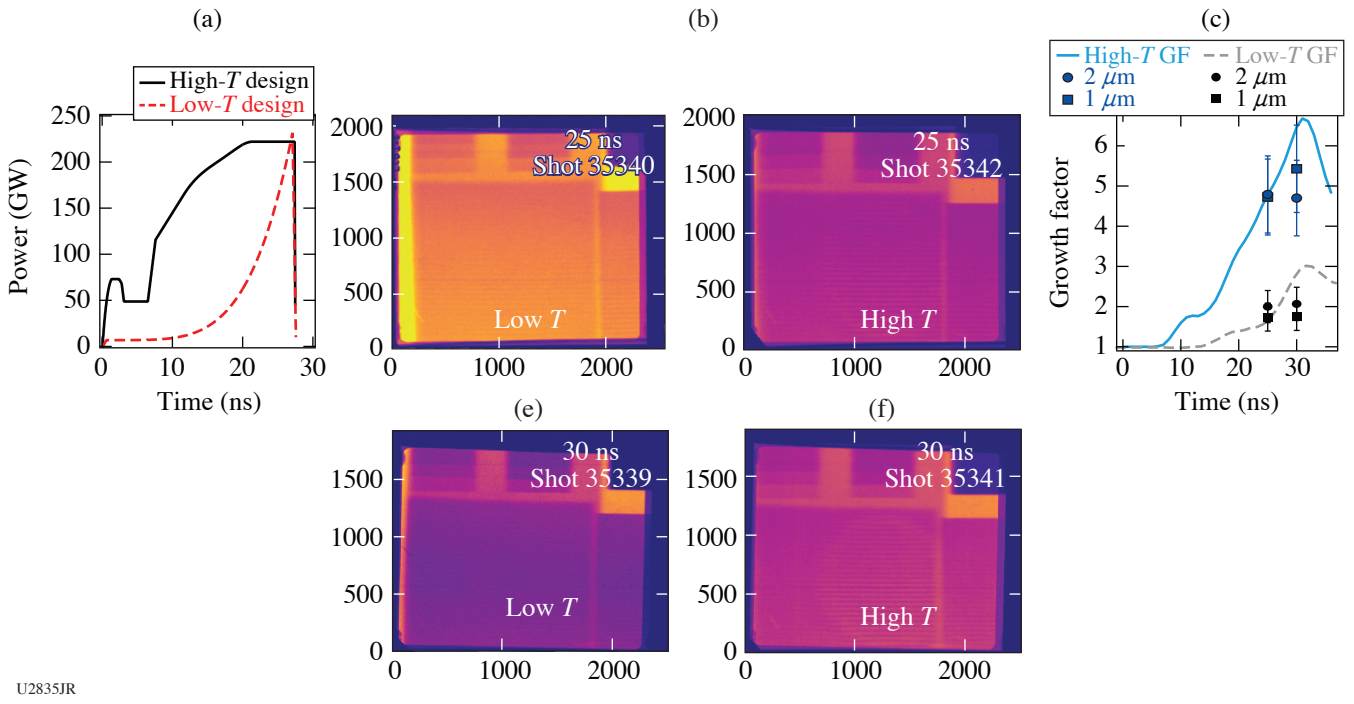

Figure 28

(a) Designed power delivery from three UV beams for high and low temperatures. The high-temperature path uses a leading shock to increase temperature rapidly, while bringing the total power and pressure peak to conditions comparable to that of the low-temperature path. (b) Radiography data collected during the shot day. (c) Preliminary calculated growth factors versus pre-shot modeling. Error bars are set to 20% of the measured value.

pusher/sample pairs. The second experiment type is platform development aimed at assessing how other pusher materials behave under similar conditions, which will inform future experiment design and model development choices.

Measuring Off-Hugoniot Equation of State by Shocking Porous Metals

Principal Investigator: A. Lazicki (LLNL)

Co-investigators: S. Jiang, F. Coppari, D. Erskine, R. London, J. Nilsen, M. MacDonald, and R. Heeter (LLNL); and M. C. Marshall (LLE)

This campaign was designed to use the crushing of pores in an initially porous sample to achieve a hot, approximately solid-density shock state. Data off of the principal Hugoniot have the potential to provide a more-discriminating test of theoretical models.

The campaign was allocated three half-days of shots in FY21. The last shot day was given some additional shots because of issues that arose with the campaign sharing the day, so we were able to collect a total of 21 shots over the year. On the first and second half-days, we measured the principal and off-Hugoniot states of gold by shocking samples of full-density and ~70% porous material (made from an Au–Ag alloy with the Ag removed), over a range of pressures. Targets with diamond ablators, an Au heat shield, and quartz impedance-matching standard were mounted on a halfraum that was driven with 21 beams along the H7–H14 axis, and shock velocity and/or transit time in adjacent samples of quartz and porous metal were measured using the VISAR and SOP diagnostics (Fig. 29). On some of the shots, a second quartz window was glued to the rear surface of the Au sample to measure the off-Hugoniot release state. On the last shot day, we measured principal and off-Hugoniot states in Cu by shocking full-density and ~50% porous Cu samples (made by powder compaction). We attempted to constrain shock temperatures by pumping x-ray fluorescence from the Cu sample surface using a Ge backlighter and measuring the spectrum using the Z-Spec spectrometer with a cylindrical crystal. The spectroscopy data suggested that multiple x-ray sources were contributing to the signal, and the VISAR and SOP data indicated that the x-ray backlighter was itself providing a significant source of heating.

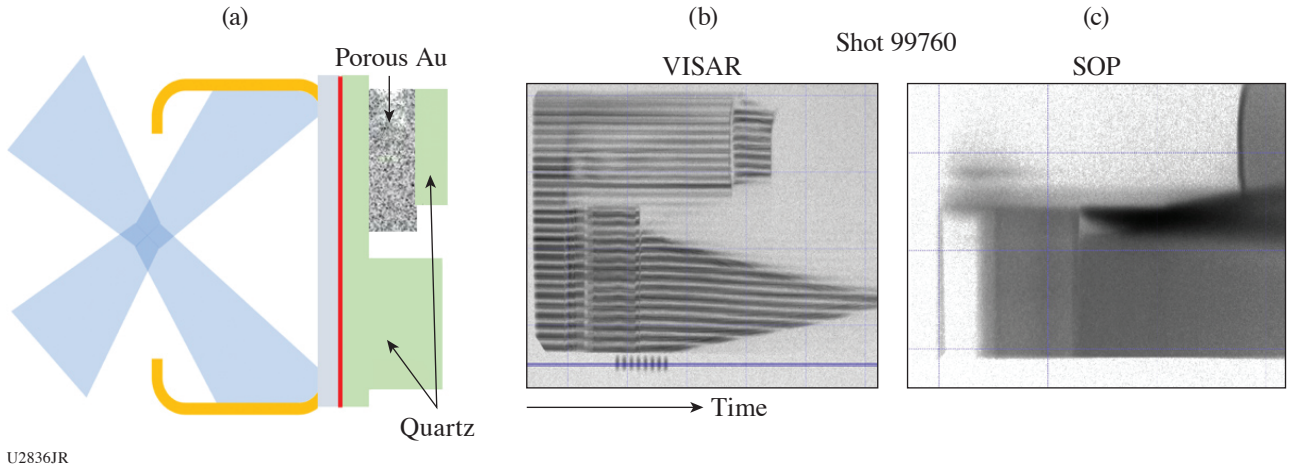

Figure 29

(a) Target configuration with VISAR and SOP data from one shot in the PorousEOS-21B Campaign, designed to measure principal- and off-Hugoniot states of Au. The VISAR diagnostic registers the *in-situ* velocity in the quartz impedance-matching standard and (b) VISAR and (c) SOP record the shock-transit time through the Au sample.

Developing X-Ray Fluorescence Spectroscopy as a Probe for High-Energy-Density Physics Experiments

Principal Investigator: M. J. MacDonald (LLNL)

Co-investigators: T. Döppner, H. A. Scott, A. M. Saunders, P. A. Sterne, K. B. Fournier, and T. Baumann (LLNL); S. R. Klein, M. P. Springstead, K. H. Ma, and C. C. Kuranz (University of Michigan); and R. W. Falcone (University of California, Berkeley)

The goal of the FoamXRFTS-20B shot day was to continue the development of a platform using simultaneous x-ray fluorescence (XRF) spectroscopy and x-ray Thomson scattering (XRTS) to measure the EOS of shocked foams. The FoamXRFTS platform

measures XRF spectra from shock-heated foams with the goal of independently measuring the plasma temperature using XRTS to benchmark atomic models for future XRF diagnostics.

In these experiments, a planar shock wave heats a cylinder of foam doped with a mid-Z element, similar to previous results published from the Trident Laser Facility,[28] with the addition of an XRTS diagnostic. A laser-driven Zn He_α backlighter both induced K-shell fluorescence from the Co-doped foam and served as the x-ray source for XRTS. A schematic of the experimental setup is shown in Fig. 30(a). The IXTS spectrometer recorded spatially resolved Co K_β XRF, providing a measurement of the density profile of the shock wave in the foam in addition to resolving XRF spectra from the shocked and unshocked regions of the foam. This campaign has successfully demonstrated the ability to measure Co K_β spectra from the shock-heated layer at a range of drive conditions with good sensitivity to the range of conditions produced, as shown in Fig. 30(b). Although the XRTS data collected in these experiments will be difficult to interpret due to noise in the data, the results will be helpful in improving the experimental setup for future campaigns. Additionally, a new conical crystal for the ZSPEC spectrometer was tested on this shot day, providing improved focusing over the 7- to 11-keV photon energy range with high collection efficiency. The conical ZSPEC will be a useful diagnostic for future x-ray spectroscopy experiments.

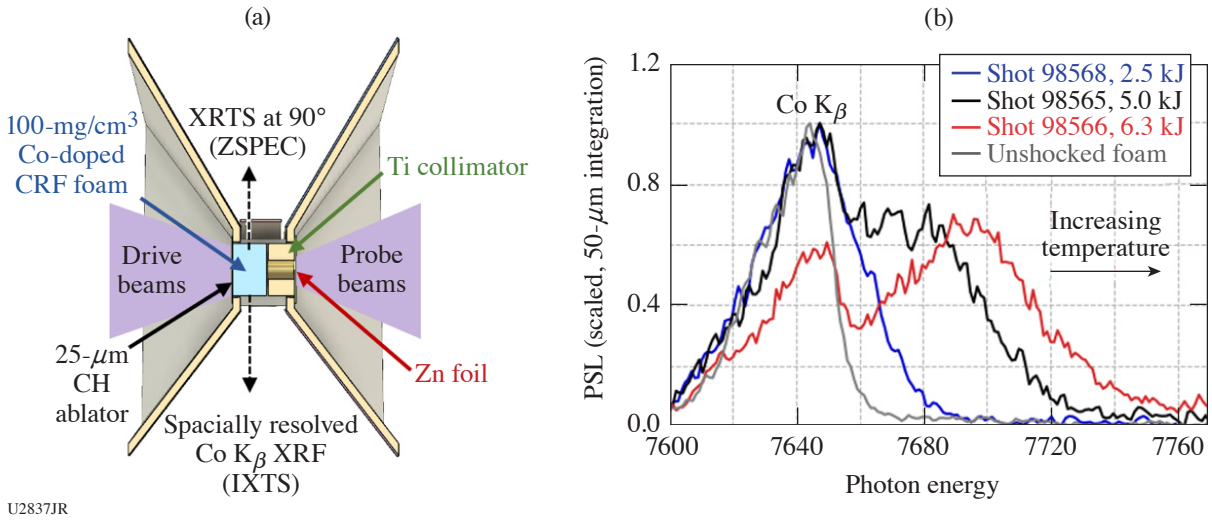

Figure 30
(a) Experimental configuration for the FoamXRFTS-20B shot day. (b) Co K_β emission spectra for the unheated foam (gray) and three drive energies, showing a strong dependence of the emission energy of the Co K_β emission with increasing drive energy and, therefore, plasma temperature.

Measurements of Release Isentropes of Proton Heated Warm Dense Matter with Streaked X-Ray Radiography
Principal Investigator: S. Jiang (LLNL)
Co-investigators: Y. Ping, A. Lazicki, A. Saunders, A. Do, D. Swift, J. Nilsen, P. A. Sterne, H. Whitley, and J. H. Eggert (LLNL); and M. P. Hill (AWE)

This campaign comprised two days on OMEGA EP during FY21. In FY20 we demonstrated that the platform can measure the release isentrope of warm dense matter that was heated isochorically with proton heating. The pressure–density isentrope was extracted from the streaked x-ray radiograph. The initial bulk temperature could be measured using SOP with a specially designed target. The spectrum and angular distribution of the proton source was recorded with a Thomson parabola and radiochromic films (RCF's). In FY21, we have successfully performed EOS measurement for Al at an ~2-eV temperature with this platform. We have also demonstrated that the heating proton beam can be focused using a hemispherical target with proximal target structures. This enables us to perform higher-temperature measurement in the future.

The experiment used the OMEGA EP short pulse to generate a beam of protons that heated a 500-μm × 50-μm × 50-μm Al ribbon offset from the proton source. Three long-pulse beams were used to heat a V backlighter to provide an x-ray source

for streaked x-ray radiography. A raw radiograph image from the PJX camera is shown in Fig. 31(a). An on-shot SOP image was also displayed that suggested heating was almost completely from the proton beam and the x-ray preheat was negligible. The measured proton spectrum suggested an energy deposition density of about 9.3×10^4 J/cm^3 in the Al sample or an initial temperature of ~2 eV. This temperature also agreed with the measured bulk temperature from SOP. The derived release isentrope shown in Fig. 31(a) agreed with both the LEOS (red) and the *SESAME* 3720 (blue) EOS tables but did not agree with the XEOS 130 table (green).

We have also designed a hemispherical proton target with a Cu guiding structure to focus the heating proton beams generated by the short pulse. The RCF images from both a regular flat foil and this hemispherical target are shown in Fig. 31(b). The hemispherical target has generated a significantly more protons and can potentially heat the sample to a much higher temperature. We will perform a temperature scan with different proton targets in future experiments.

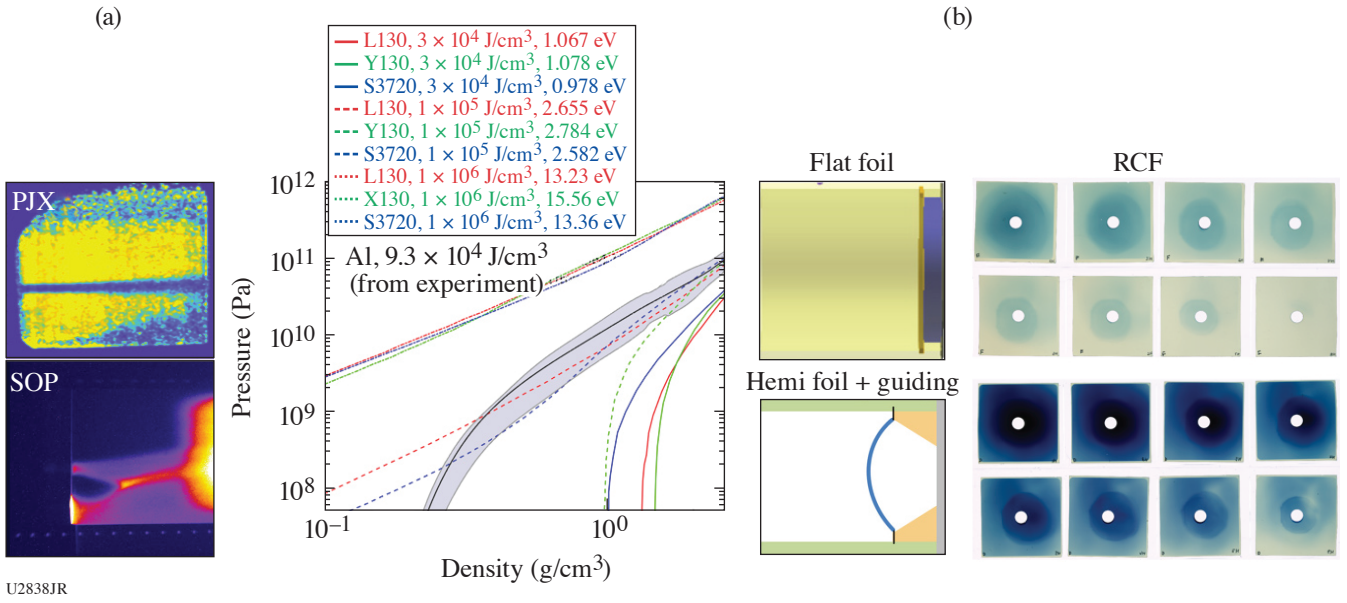

Figure 31
(a) Streaked radiograph, SOP data, and the extracted pressure–density isentrope curve. Isentrope curves from various EOS models at different energy densities/initial temperatures were also plotted for comparison. (b) RCF images of the proton beams generated by two different proton targets with the same laser pulse.

Laser-Driven Accelerated Diamond Flyer Plates for Absolute Equation-of-State Measurements

Principal Investigator: F. Coppari
Co-investigators: A. Lazicki, M. Millot, R. London, R. Heeter, and D. Braun

In order to characterize material EOS at HED conditions, there is a need for developing appropriate pressure standards. The goal here is to develop a platform for performing reference-free EOS measurements of materials in the multi-Mbar regime to be used as an absolutely calibrated pressure standard in future EOS measurements.

We were allocated one day on the OMEGA EP laser and conducted seven experiments, where we accelerated a diamond flyer plate to an increasingly high velocity across a vacuum gap of known thickness. We used the VISAR diagnostic to observe the impact of the flyer onto a diamond window. VISAR provided a measure of the flyer velocity before the impact. From that, considering the impact is symmetric, the particle velocity can be obtained. After the impact, the VISAR recorded the shock velocity [Fig. 32(a)]. From these two observables the pressure–density relation of diamond can be obtained by solving the Rankine–Hugoniot equations.[29]

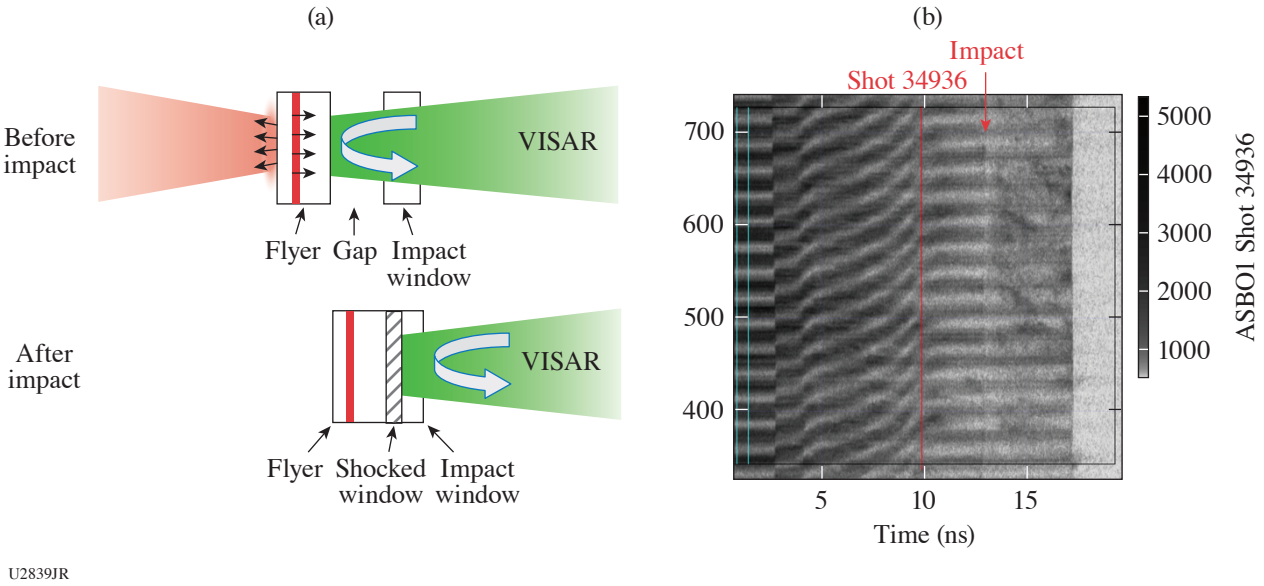

Figure 32
(a) Schematic showing the experimental concept and measurement. Lasers accelerate a diamond flyer across a vacuum gap, and VISAR is used to measure the flyer velocity before the impact and the shock velocity after the impact. (b) Representative VISAR data where a diamond flyer was accelerated to high velocity near 30 km/s. After the impact (red arrow), the fringe pattern is not so clear, preventing determination of the shock velocity.

A tailored-ramped pulse shape was used to slowly accelerate the flyer up to peak velocity, avoiding melting and keeping its density close to ambient density. Depending on the flyer velocity, the impact might generate a reflecting shock in the diamond window when the propagated shock is strong enough to melt the window.

During this campaign we varied the laser energy to span pressures across the diamond-melting transition. As pressure was increased, the VISAR record showed increased loss of reflectivity and nonuniformities pointing to the possibility that the diamond flyer may break up before the impact, providing an unreliable velocity measurement [Fig. 32(b)].

These issues are currently under evaluation, and they will have to be addressed before we can establish diamond as an absolute standard for equations of state measurements.

Outputs and Survivability Campaigns

Studying Electrostatic Discharge in Solar Cell Arrays Under Extreme X-Ray Irradiation
Principal Investigator: K. Widmann (LLNL)
Co-investigators: P. L. Poole, J. Emig, and B. E. Blue (LLNL); S. Seiler (Defense Threat Reduction Agency); S. Burnham (Air Force Research Academy); and J. Lorentzen, D. Scheiman, and P. Adamson (Naval Research Laboratory)

The SolarCellESD campaign seeks to determine experimentally whether prompt x rays can induce failure modes in solar arrays that are not accounted for by simply testing the individual solar cells alone because the voltage difference between neighboring cells can be hundreds of volts, depending on the overall layout of the array. These experiments on OMEGA have been fielding the smallest-possible array; i.e., 2 × 1 cells with electronic controls that allow the user to dial in a voltage difference (bias voltage) between the two cells and, therefore, to study the failure modes as a function of incident x-ray flux and bias voltage (Fig. 33). Previous campaigns have studied various shielding techniques, the addition of magnets to deflect charged-particle winds, and adjustments to the laser-driven x-ray source.

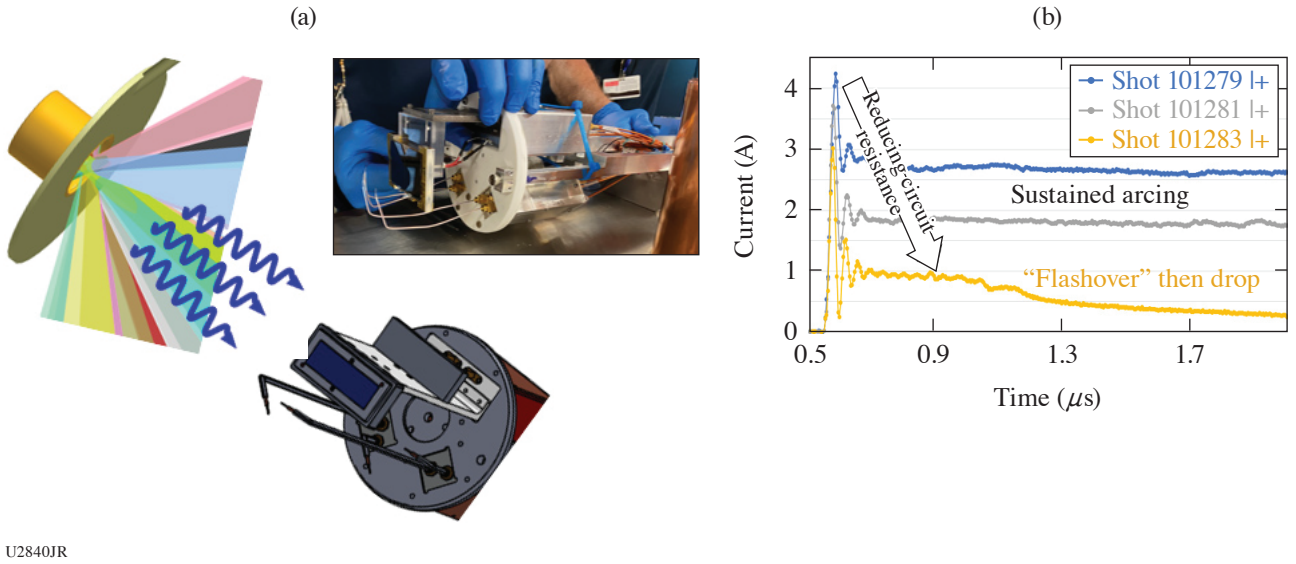

Figure 33
(a) A solar cell array (2 × 1) is held within the x-ray Langmuir probe diagnostic at variable standoff distances from a laser-driven hohlraum x-ray source. A variable bias voltage is placed between the cells to simulate working conditions. (b) Voltage characteristics indicative of sustained arcing were observed on this shot day to be controllable by resistance changes within the solar cell circuitry.

The FY21 shot day fielded solar cells in two TIM's with similar viewing angles on either side of a hohlraum x-ray source such that one could be used as a control while parameters such as the bias voltage, standoff, or circuit resistance were varied on the other. A hot hohlraum target was also used on this day to increase the x-ray fluence on the cells. The threshold fluence for sustained arcing was observed, while subsequent shots charting the arcing behavior as resistors were removed from the circuitry behind the solar cells. These data provide critical benchmarks that will build up on the utility this campaign has provided to in-use solar cell arrays on satellites.

Investigating Bremsstrahlung X-Ray Source via Magnetic Fields
Principal Investigator: P. L. Poole
Co-investigators: R. K. Kirkwood, S. C. Wilks, M. May, K. Widmann, and B. E. Blue

High-fluence x-ray sources can be used to test for extreme radiation environment effects[30] including nuclear survivability. Facilities like the NIF and Z can readily produce high fluences of x rays under 10 to 20 keV, but high-photon-energy versions of those line-emission–dominated sources are considerably weaker. The SRSxray Campaign on OMEGA investigates a different x-ray–generation mechanism that produces a bremsstrahlung spectrum using the hot electrons accelerated from strong plasma waves within the target.

In this campaign, two MIFEDS coils were utilized to generate an axial magnetic field within gold hohlraums; these fields serve to confine plasma flow and prolong the temperature and density conditions conducive to laser–plasma interactions (LPI's) that drive this x-ray source. Here, multiple wall thicknesses were used to assess the effects of B-field penetration to the plasma as well as variations in the low-density CH foam fills that have been developed on past days to enhance desired LPI. Figure 34(a) shows thicker targets enhancing the x-ray output in the desired >50-keV range when the magnetic fields are off but with an output enhancement for thinner walls when the B field is present. These results help scale the trade-off between the B-field penetration and the greater attenuation of exiting x-ray radiation from the source.

Additionally, Fig. 34(b) shows backscattered light from two target configurations where this signal is strongly suppressed when the magnetic fields are present. This is in line with simulations[31] and also suggests the plasma flow is constrained but still produces

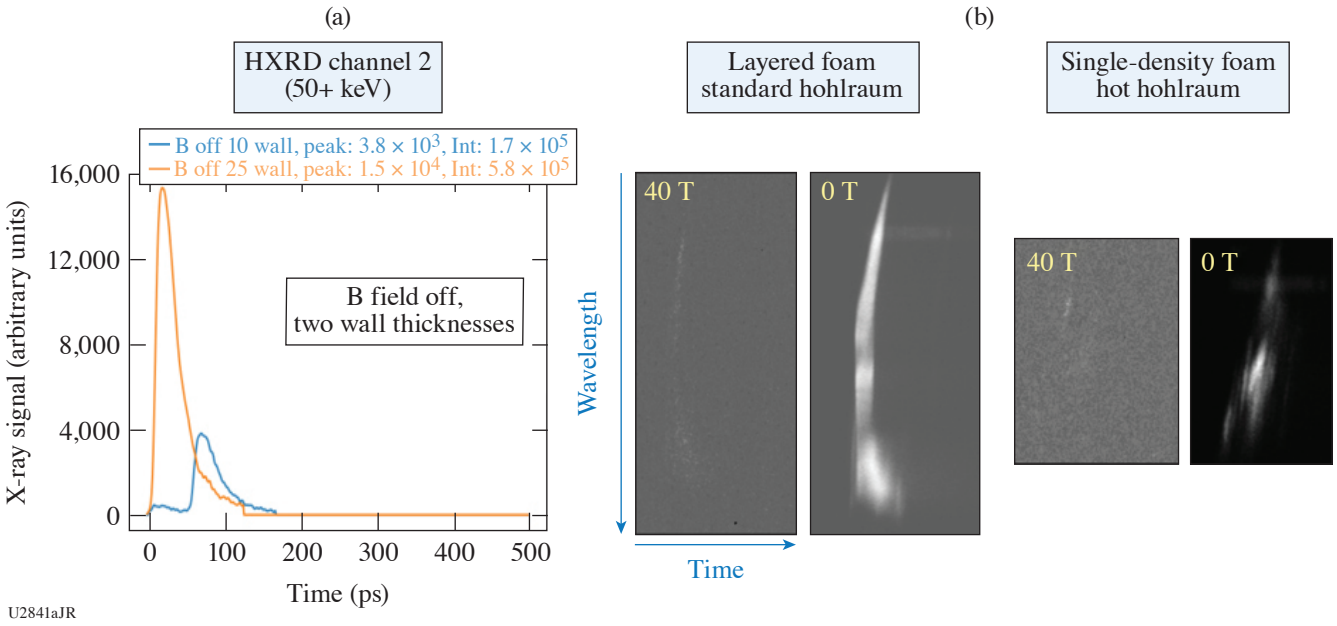

Figure 34
(a) X-ray signal from channel 2 (≳50-keV photons) for two different hohlraum wall thicknesses, showing a strong increase for the thicker option (B field off here). (b) Streak camera data for SRS wavelengths show a reduction in backscattered light when strong B fields are present.

hot electrons relevant to increased x-ray bremsstrahlung output. These findings are instrumental to the design of upcoming NIF shots with magnetic fields intended to enhance this x-ray source.

Comparing CH and HDC Exploding-Pusher Performance

Principal Investigator: M. Hohenberger (LLNL)
Co-investigators: P. W. McKenty and M. J. Rosenberg (LLE); and L. Divol, C. B. Yeamans, B. E. Blue, and W. W. Hsing (LLNL)

Experiments were conducted to directly compare nuclear yield and performance of exploding-pusher (XP) targets with CH and HDC ablators. The nuclear yield in XP's primarily stems from shock heating of the fusionable fill gas, and these implosions exhibit low convergence, low areal densities, and high ion temperatures. By virtue of their shock-driven nature, XP's are insensitive to degradation mechanisms that affect high-convergence implosions, such as electron preheat or RT instabilities. While yield amplification or a propagating burn is not accessible at these conditions, significant neutron yields >10^{16} have been demonstrated on the NIF, making XP's robust sources for, e.g., nuclear effects studies or backlighters.[32] Many of these applications greatly benefit from increased nuclear fluence, and increasing XP performance is a key programmatic goal. XP's fielded on the NIF are typically CH capsules, but HDC has been identified as a potentially interesting ablator material with simulations predicting increased absorption efficiency and therefore higher nuclear yields.

To test this experimentally, 860-μm-diam HDC and CH targets filled with room-temperature D_2 gas at 8 atm were symmetrically imploded with 60 OMEGA beams (~400 J/beam, 1-ns square). The targets were mass-matched featuring 4-μm- and 12-μm-thick walls, respectively. CH capsules were diffusion filled and mounted via an 18-μm stalk, while the nonpermeable HDC capsules required a 70-μm fill tube. Experimental data for the CH (circle) and HDC (diamond) are shown in Fig. 35. Notably, the CH yield is comparably robust varying between 3.6 and 4.2 × 10^{11}, while HDC exhibits significant variation for the two shots, either below (2.9 × 10^{11}) or matching (4.0 × 10^{11}) the CH. In contrast, the bang time is consistent for both HDC experiments and ~50 ps earlier than for the CH. A possible explanation for these data is the perturbation imposed by the fill tube and glue spot unique to the HDC design. Self-emission x-ray images of the HDC implosions exhibit a noticeable "ring" feature, which lines up with the expected position of the fill tube. No such feature is visible in the CH data. It is likely this caused detrimental mix

and capsule breakup for the HDC, thus limiting performance. The fact that one HDC implosion matched the CH performance despite this issue is a promising result, and future experiments will test a "fill-and-plug" design, with HDC capsules prefilled through a small hole. This is then plugged prior to fielding the capsule, thus sealing in the gas fill and causing a much smaller perturbation to the implosion.

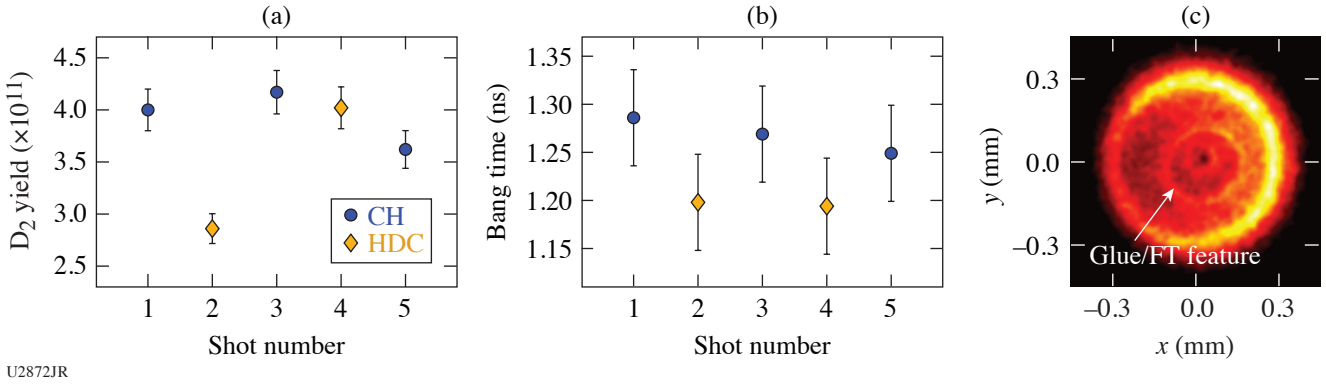

Figure 35
(a) Experiments comparing HDC (diamond) and CH (circle) ablator performance in exploding-pusher implosions saw no yield improvement for the HDC. (b) HDC implosions exhibited a consistently earlier bang time. (c) Self-emission data of HDC implosion at 0.6 ns show a perturbation attributed to the fill tube and glue spot unique to the HDC design. No such feature can be seen in CH data.

Collisionless Shocks Produced in Magnetized Plasmas

Principal Investigator: E. Tubman (LLNL)
Co-investigators: B. Pollock, G. Swadling, D. Higginson, D. Larson, B. E. Blue, and H.-S. Park (LLNL); M. Manuel (GA); and P. Tzeferacos and K. Moczulski (University of Rochester)

This campaign sets out to investigate high-altitude nuclear explosions (HANE's) using the Omega Laser facility. HANE's conducted by both the USA and USSR between 1958 and 1962 sent out shock waves that created long-lasting radiation belts of high-energy, charged particles.[33] Satellites close to these events experienced substantial radiation damage, and the effects were even observed at the Earth's surface, such as in Hawaii where street lighting was affected. Computer simulations are not entirely accurate in modeling certain aspects of the HANE's, in particular the mechanism via which the radiation belts are formed. The Omega Laser Facility provides an ideal environment in which to produce collisionless shocks within magnetized, low-density plasma environments and assist in our understanding of the early-time evolution of HANE's and better inform our codes.[34]

To field this experiment at the Omega Facility requires several different target components. First, a low-density, magnetized plasma "background" region is created using a hydrogen gas jet, within a MIFEDS Helmholtz coil setup. The gas jet produces a density of $\sim 10^{18}$ cm^{-3} and the MIFEDS themselves provide an ~10-T field. The central region of the MIFEDS, where the gas is present, is irradiated with five laser beams producing an ionized, magnetized plasma. Then, after 6 ns to allow the background plasma to reduce in temperature, a second group of laser beams with $I \sim 5 \times 10^{14}$ W/cm^2 impact on a "piston" drive target composed of beryllium. This drives a high $M_A > 5$ shock from the front side of the target. The aim is to generate a collisionless shock coupled to the magnetized background ions. The shock, as it propagates outward, is expected to sweep up field, and a diamagnetic cavity may form at its front due to the large debris ion gyroradius and the low ambient plasma density.[35] Proton imaging, driven using the OMEGA EP beam, allows one to measure the magnetic-field structures, and a 2ω probe beam is used for Thomson scattering, enabling the plasma T_e, T_i, n_e, and flow velocity to be calculated. The setup for this experiment is shown in Fig. 36(a).

Figures 36(b) and 36(c) show radiograph images produced by the protons passing through the magnetic fields 4 ns after the drive beams have started ablating material from the Be target. Figure 36(b) shows a potential shock structure appearing (darker line) between two bubble-like voids. For this shot, the RCF contains many features and needs further analysis to confirm the

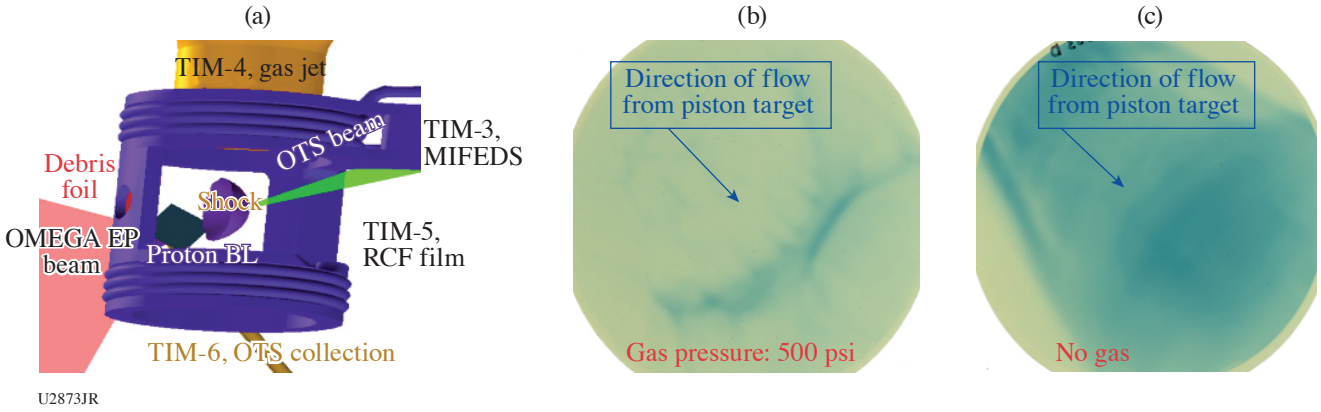

Figure 36
(a) A schematic of the setup for the experiment. The shock propagates from the front side of the target into the region of pre-ionized, premagnetized gas. (b) An RCF image of the shock driven from the piston target located in the top left (out of view) and propagates to bottom right, through a background plasma. (c) An RCF slice with no gas jet present where plasma is driven from the piston target through the magnetic fields produced by the MIFEDS.

structures observed. Figure 36(c) shows the field structure of the MIFEDS when no gas is present. Plasma will have been ablated from the piston target in the top left of the image and expanded outward; however, without the background gas, a shock feature is not observed.

In addition to the proton mapping of the fields, Thomson-scattering data were also collected for shots with and without a background gas. The results are shown in Fig. 37. The IAW scatter allows one to measure the flow velocities as well as temperatures and densities. The latter of these parameters will be further corroborated using the results from the electron plasma wave. The Thomson-scattering volume is located at the center of the MIFEDS coils and can be used to measure when the shock wave passes across this region. Figure 37(b) shows that no scatter is observed from this central region at earlier time (<2.5 ns after the beams are incident on the piston target) and the only signal at this time comes from stray light at the probe-laser wavelength. After 2.5 ns, we do see IAW scatter, and preliminary analysis of the features suggest that without the presence of a magnetized background plasma, the piston material propagates out with velocities of $v \sim 1500$ km/s. When a backing gas-jet pressure of ~100 psi is used, the piston material is slowed to ~1100 km/s [Fig. 37(a)]. Material behind the front of the plasma flow then decreases in both cases, as shown by the gradient in the scattered wavelength, tending back to the original probe wavelength. These measurements can be compared to the hydrodynamic simulations run using *HYDRA*. For the no-gas case, they match well with predictions. Further analysis will be completed on this data and will help to inform future shot days where we will also investigate the effects of driving shocks from diamond targets.

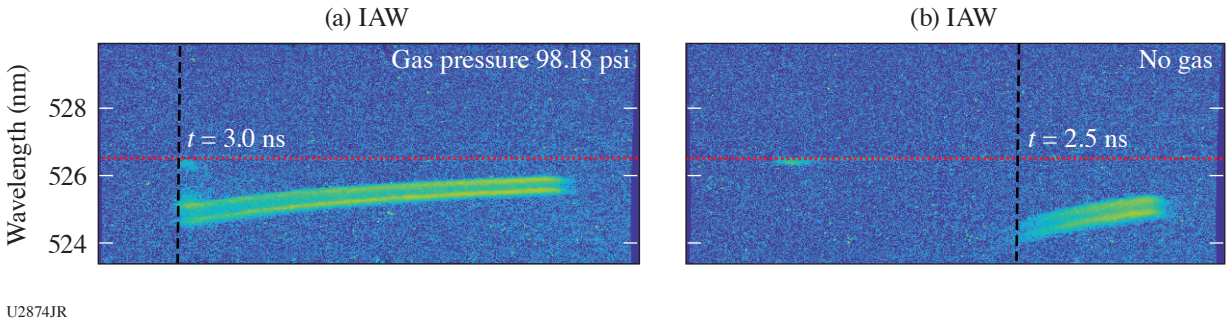

Figure 37
(a) The ion-acoustic feature from Thomson scattering shows material present in the central region of interest 3 ns after the lasers are incident on the piston target. The gas-jet backing pressure was ~100 psi. (b) The ion-acoustic feature shows faster propagation velocities when the piston target material propagates out into only vacuum (no gas jet present).

1. *LLE 1999 Annual Report, October 1998–September 1999*, 222, Rochester, NY, LLE Document No. DOE/SF/19460-332 (2000).

2. J. H. Eggert *et al.*, Nat. Phys. **6**, 40 (2010).

3. M. Millot *et al.*, Phys. Plasmas **27**, 102711 (2020).

4. S. Le Pape *et al.*, Phys. Rev. Lett. **120**, 245003 (2018).

5. M. Millot *et al.*, Phys. Rev. B **97**, 144108 (2018).

6. W. A. Farmer *et al.*, Phys. Plasmas **27**, 082701 (2020).

7. C. Goyon *et al.*, Phys. Rev. E **95**, 033208 (2017).

8. J. J. Santos *et al.*, New J. Phys. **17**, 083051 (2015).

9. H. Daido *et al.*, Phys. Rev. Lett. **56**, 846 (1986).

10. K. F. F. Law *et al.*, Appl. Phys. Lett. **108**, 091104 (2016).

11. G. J. Williams *et al.*, J. Appl. Phys. **127**, 083302 (2020).

12. C. Goyon *et al.*, Phys. Rev. E **95**, 033208 (2017).

13. R. A. Simpson *et al.*, Phys. Plasmas **28**, 013108 (2021).

14. G. G. Scott *et al.*, Rev. Sci. Instrum. **93**, 043006. (2022).

15. C. Courtois *et al.*, Phys. Plasmas **28**, 073301 (2021).

16. D. R. Rusby *et al.*, Bull. Am. Phys. Soc. **66** (2021).

17. A. M. Saunders *et al.*, Phys. Rev. Lett. **127**, 155002 (2021).

18. M. C. Marshall *et al.*, J. Appl. Phys. **127**, 185901 (2020).

19. D. E. Fratanduono *et al.*, Science **372**, 1063 (2021).

20. J. R. Rygg *et al.*, Rev. Sci. Instrum. **91**, 043902 (2020).

21. N. Dubrovinskaia *et al.*, Sci. Adv. **2**, e1600341 (2016).

22. A. Dewaele *et al.*, Nat. Commun. **9**, 2913 (2018).

23. N. A. Smirnov, J. Phys.: Condens. Matter **29**, 105402 (2017).

24. R. Briggs *et al.*, Phys. Rev. Lett. **123**, 045701 (2019).

25. S. K. Han *et al.*, Phys. Rev. B **103**, 184109 (2021).

26. E. J. Gamboa *et al.*, Rev. Sci. Instrum. **83**, 10E108 (2012).

27. A. Do *et al.*, Rev. Sci. Instrum. **91**, 086101 (2020).

28. M. J. MacDonald *et al.*, J. Appl. Phys. **120**, 125901 (2016).

29. Ya. B. Zel'dovich and Yu. P. Raizer, *Physics of Shock Waves and High-Temperature Hydrodynamic Phenomena*, edited by W. D. Hayes and R. F. Probstein (Dover, Mineola, NY, 2002).

30. M. J. May *et al.*, Phys. Plasmas **25**, 056302 (2018).

31. B. J. Winjum *et al.*, Phys. Rev. E **98**, 043208 (2018).

32. C. B. Yeamans *et al.*, Nucl. Fusion **61**, 046031 (2021).

33. C. E. McIlwain, Science **142**, 355 (1963).

34. D. B. Schaeffer *et al.*, Phys. Rev. Lett. **119**, 025001 (2017).

35. D. S. Clark *et al.*, Phys. Plasmas **20**, 056318 (2013).